4.4 Bunch Compressor

4.4.1 Introduction

A higher luminosity can be obtained with a given beam emittance by making the beta function at the collision point smaller but, if the beta function becomes about the same as the bunch length, one cannot increase the luminosity any more. Thus, a short bunch is needed for higher luminosity. It also helps to minimize the adverse effect of short-range wake field in the main linac. The proposed beam parameters of JLC-I (Sec. 4.1) require the bunch length ranging from 80 μm to 150 μm in the main linacs. The bunch length in the 1.98 GeV damping ring (DR) is about 5 mm and the energy spread is 0.93×10^{-3}. Thus a compression of bunch length by a factor of 63 is required. Due to the emittance preservation in longitudinal phase space, this process causes an increase of the energy spread by the same factor, which cannot be accepted by the main linac and by the compressor itself. It is therefore necessary to have a system composed of two compressors between which an intermediate linac (pre-linac) accelerates the beam to recover the relative energy spread within bearable values.

In the following sections, the number of particles in a bunch (N) and the number of bunches in a train (m_b) are assumed to be $(0.7 \sim 2) \times 10^{10}$ and $50 \sim 80$ respectively, while preserving their total charges to be 8×10^{11} in a train.

4.4.2 Basic parameters

In this section we discuss the choice of the beam energy at the second compressor and the compression factors of the first and the second compressors. Key issue is the energy spread in each stage. We have to consider two points. Firstly, the multi-bunch beam loading in DR, if not compensated within DR, brings about unequal equilibrium distances between the bunches. These deviated positions are mapped to different energies at the exit of the first compressor (referred to as BC1 hereafter) which performs a 90° phase rotation in the longitudinal plane. The position deviation amounts up to 5 mm ($1\sigma_z$(DR)) for the proposed DR cavity. It is converted to an energy shift $1\sigma_\epsilon$ at the cavity of BC1. Secondly the acceleration in the pre-linac yields an energy spread due to the single-bunch beam loading. With S-band structures, the rms energy spread is approximately 0.2% for $N = 2 \times 10^{10}$ and σ_z=0.5mm [28].

Fig 4.28 shows the energy spread (2σ) in the BC1 and BC2 as a function of the compression factor of BC1 for various energies of BC2. We have assumed a compensation of multi-bunch energy shifts at the entrance of the pre-linac (S-band). The solid line of BC1 is the energy spread at the entrance of the S-band linac, while the broken line shows that in the second arc of BC1. We have also included weak dependence of single-bunch energy spread in the linac on the bunch length. The multi-bunch energy spread in the S-band linac is assumed to be 0.15% (peak-to-peak). A higher energy of BC2 relaxes the energy spread of BC1 and BC2. There must be a trade-off between the cost of the pre-linac and the difficulties of the transport in BC2 and in the first portion of the linacs. In the following we choose the energy of 20 GeV. The energy spread ($\pm 2\sigma$) at the entrance of pre- and main linac is $\pm 2.58\%$ while at the second arc of BC1 it is $\pm 2.58\% \times 3/2 = \pm 3.87\%$. The compression factors of BC1 and BC2 are 0.072 and 0.222, respectively. Table 4.9 shows the basic parameters of the bunch compressors. Fig 4.29 shows a schematic view of the bunch compressor sysytem.

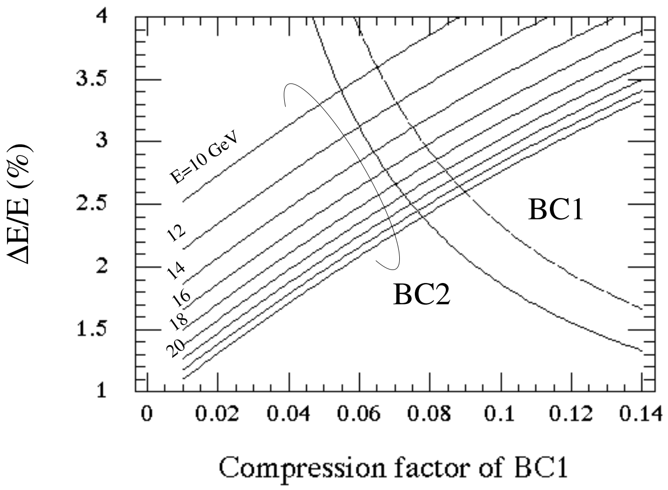

Figure 4.28: Energy spread of bunches (in 2σ) versus compression factor of the first compressor.

Table 4.9: Basic parameters of bunch compressors

Location	Energy spread(2σ) (%)	Bunch length (mm)
Damping Ring	0.186	5.0
BC1 (second arc)	3.23	$5.0 \rightarrow 0.36$
BC1 (exit)	2.58	0.36
S-band Linac	$2.58 \rightarrow 0.570$	0.36
BC2 (exit)	2.56	0.08

4.4.3 First Compressor

There are two issues which should be taken into consideration in the design of the first bunch compressor (BC1). Both of them are related with the multi-bunch beam-loading effect. Firstly, the beam-loading in the damping ring causes unequal displacements among the bunches in a train, which can result in unequal acceleration in the linac, if the beam is directly injected to the linac. Actually, however, this will make no problem since the longitudinal phase advance 90° of the bunch compressor converts the position shift to an initial energy spread in the linac (Fig. 4.30(a)) which eventually fades out during acceleration. Secondly, the transient beam-loading in the cavity of the bunch compressor itself produces an energy spread among bunches. This brings about an incomplete rotation in the longitudinal phase space, resulting in different longitudinal positions in the linacs which cause an energy spread again (Fig. 4.30(b)).

The parameters of BC1 are summarized in Table 4.10.

Longitudinal optics of BC1

These linear or nonlinear position shifts in the DR are converted by BC1 to energy shifts in the following linacs. The condition of 90° phase advance and that of upright ellipses at the both ends give

$$\ell_1 = \ell_2 = -1/k = m_1\beta_1 = m_1\sigma_{z_0}/\sigma_{\epsilon_0} \ , \tag{4.17}$$

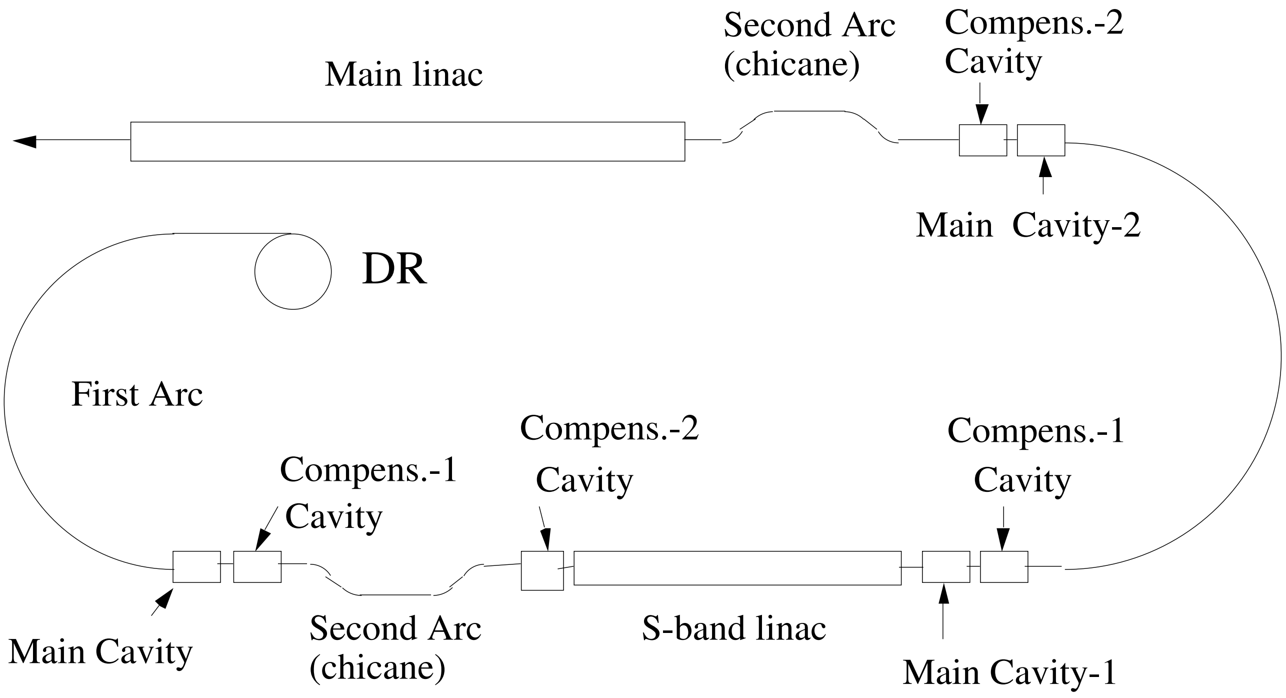

Figure 4.29: Schematic view of bunch compressor system

where $\ell_i (i = 1, 2)$ are the dilation factors of the arcs before and after the cavity, k is the local slope of the RF voltage normalized to the nominal energy, and m_1 is the compression factor of BC1. In the present design $\ell_1 = \ell_2 = 0.387$ m and $\hat{V} = 170.9$ MV for the L-band cavity structure. The energy shift after passing the compressor cavity becomes 1.29 %. Adding 2σ energy spread of single bunch to this, we find the required band width of the second arc to be $\pm 3.24\%$.

Second arc of BC1

It is essential to transport the beam with such a tremendous energy spread of $\pm 3.5\%$. The usual achromat system seems impossible to apply. We adopt a chicane section instead of arc[30].

Table 4.10: Parameters of the first bunch compressor

Momentum compaction of first arc	ℓ_1	0.387	m
Momentum compaction of second arc	ℓ_2	0.387	m
Main cavity voltage	V_M	171	MV
frequency	f_0	1.428	GHz
Compensation-1 voltage	V_{C1}	61.0	MV
frequency	f_{C1}	1.428	GHz
beat frequency	Δf	0.25	MHz
Compensation-2 voltage	V_{C2}	62.5	MV
frequency	f_{C2}	2.856	GHz
beat frequency	Δf	0.25	MHz

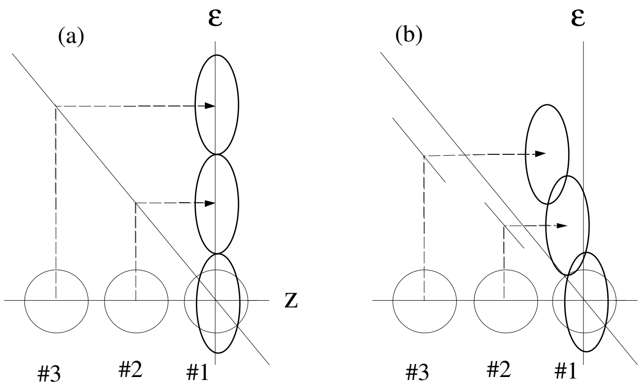

Figure 4.30: Beam-loading effects in Bunch Compressor: (a) position shifts in DR are converted to energy shifts by the compressor, (b) beam loading in the compressor cavity produces an incomplete rotation in the (z,ϵ) space.

Since the section has no quadrupole, it has no chromatic effect in principle. Furthermore it has no high order dispersion at the exit. We have checked the fringe effect that possibly leaks the horizontal emittance to the vertical plane and found that a large bending radius suffices to suppress the leakage. The total length of the chicane is 20 m, each bend being 2.2 m in length with the bending radius 8.25 m. We have made a tracking simulation and found that the vertical emittance increases by 3% due to bending magnet errors: the rotation error of 0.1 mrad, the vertical misalignment of 0.1 mm, and the sextupole component of 0.1% of the main field.

4.4.4 Second Compressor

We assume the multi-bunch energy compensation in the S-band linac is possible within 0.15%. It is essential to prevent this energy spread from being converted to a position spread in the main linac which results in a non-uniform acceleration of bunches. Thus, we adopt 180° phase advance in BC2, which can be realized by two cavities.

A chicane section can be used for the second arc as in the first compressor. In this case emittance growth due to synchrotron radiation should be carefully taken into account. Four bends comprise a chicane with a bending field of 0.2 T. Each bending magnet has a length of 13.1 m. It is quite important that the input beam ellipse matches the beam ellipse generated by the synchrotron radiation; otherwise the radiation would produce a larger emittance growth due to the mismatch in the betatron phase space. A multiple chicane is not usable from the viewpoiont of matching. The maximum dispersion function amounts to 0.71 m. A simulation showed that the emittance growth is 5 % at most. We checked a possible emittance growth in the vertical plane due to the edge field by a tracking calculation. We found that a rotation error of 0.5 mrad yields the emittance growth of 3 %. A relative sextupole field component of 1×10^{-3} at 3 cm in the horizontal position does not give any significant emittance growth.

The parameters of the second compressor are given in Table 4.11.

Table 4.11: Parameters of the second bunch compressor

Momentum compaction of first arc	ℓ_1	0.191	m
Momentum compaction of second arc	ℓ_2	0.0425	m
Main cavity–1 voltage	V_{M1}	534	MV
Main cavity–2 voltage	V_{M2}	2401	MV
frequency	f_0	11.4	GHz
Compensation-1 voltage	V_{C1}	1380	MV
frequency	f_{C1}	11.4	GHz
beat frequency	Δf	0.25	MHz
Compensation-2 voltage	V_{C2}	3552	MV
frequency	f_{C2}	11.4	GHz
beat frequency	Δf	0.25	MHz

4.4.5 Beam-Loading and Its Compensation

Equilibrium phases in the damping ring

Since the azimuthal bunch distribution in the damping ring is not uniform because of the gaps between the trains, each bunch feels different accumulated wake field of the fumdamental mode. The tail bunches feel larger wake than the preceding bunches do. Since the bunch energy must be the same, the consequence of the different loaded voltage is a different equilibrium position among bunches. The calculation result is shown in Fig. 4.31. If only the fundamental mode is taken into account, the position shift is almost linear in the bunch number and it amounts to 5 mm. In Fig. 4.31(b) we included a higher-order mode with $Q = 300$ whose frequency accidentally coincides with 4.5 times the fundamental one. This means the wake of a bunch accelerates the next bunch, decelerates the second next, and so forth. Thus, depending on how many bunches are ahead, the bunch position staggers around the line determined by the fundamental mode wake. This staggering position shift, however, has no sizable effect on the compensation described in the following, since they are small compared to the bunch length.

Compensation of the beam-loading in the compressor cavities

The beam-loading voltage at the last bunch in BC1, for example, is estimated as 13.8 MV for the L-band structures with the structure length of 11 m and the loss parameter per unit length of 4.75 V/pC/m scaled from S-band. This is comparable to the energy gain of the last bunch of 25.6 MeV, assuming the middle bunch is placed at the zero-cross phase of the compressor cavity. Since the following bunches are at the crest of the beam-loading voltage, it cannot be compensated for by adjusting the main compressor voltage. The energy gain of a particle at the center of the n-th bunch z_n is expressed by

$$\begin{aligned} V_n &= V_0 \sin[k_0(z_n + z) + \psi] - V_b(n) \\ V_b(n) &= 2kq \textstyle\sum_{i=1}^{n-1} [L - (n-i)\Delta s] \cos k_0(z_n - z_i) \ , \end{aligned} \tag{4.18}$$

where $V_b(n)$ is the beam-loading voltage at the n-th bunch. Here, we assumed a simple constant-impedance structure. L is the total structure length and Δs the propagation length of RF power

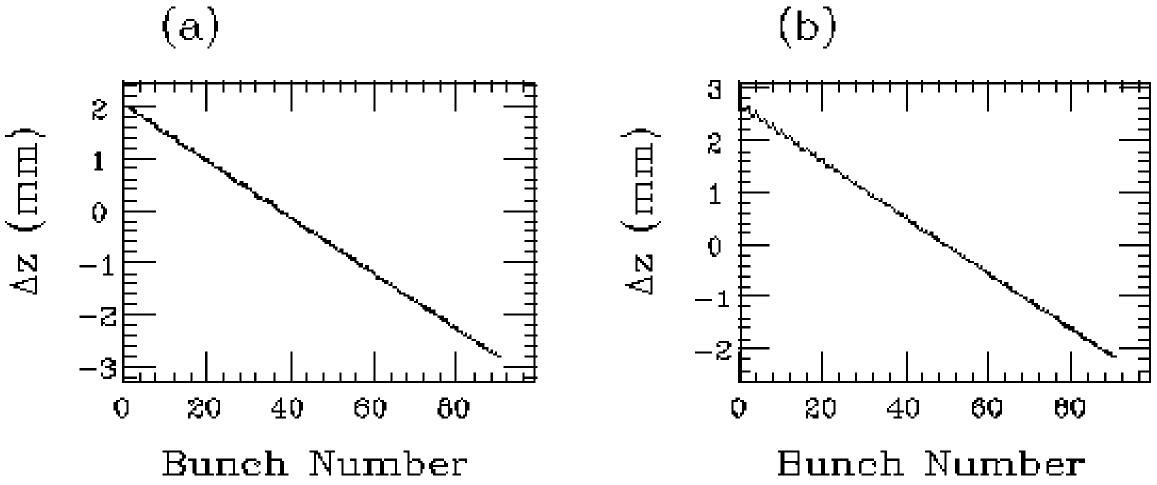

Figure 4.31: The equilibrium position in DR: (a) with the fundamental mode only and (b) including a higher order mode(HOM). The loss parameter of HOM is equal to that of the fundamental mode. Q(HOM)=300, f(HOM)=$4.5f_0$.

between two successive bunches. In our design, the number of bunches m_b is rather large (50 to 90), meaning that the quadratic term in n in Eq. (4.18) is not negligible.

To compensate for the beam loading, it is desirable to use a steady-state of a structure. A conceivable compensation scheme is to use two structures driven by slightly different frequencies. The principle is shown in Fig. 4.32. Denoting the wave numbers as $k_0 \pm \Delta k$, one can write the

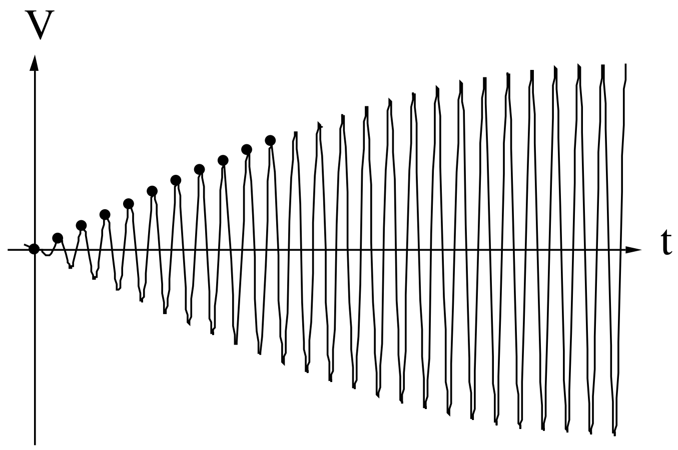

Figure 4.32: Beating method. Each bunch is placed on the crest of modulated rf.

summed voltage as

$$\begin{aligned} \Delta V_n &= V\sin[(k_0+\Delta k)z_n+\phi] - V\sin[(k_0-\Delta k)z_n+\phi] - V_b(n) \\ &= 2V\sin(\Delta k z_n+\phi)\cos k_0 z_n - V_b(n), \end{aligned} \tag{4.19}$$

where $\phi = 2\pi(\Delta k/k_0) \times$ integer is assumed. $V_b(n)$ is the beam loading of the compensation cavity itself. By adjusting the beat phase ϕ and the amplitude V, the beam-loading voltages of the main and the compensation cavities can be cancelled up to the second order in n.

This method can correct the energy deviation of bunches up to the second order without affecting the single bunch energy spread. We attach this compensation system to each main cavity in the compressors. It is also adopted at the exit of BC1 to compensate for the energy shift which is converted from the position shift in DR.

The heavy beam-loading generates energy and position shifts in the second compressor, too. The beam loading in the first cavity produces an energy shift since the phase advance is 180°, while that in the second cavity yields mainly a position shift since the phase advance between the second cavity and the exit of BC2 is almost 90°. These effects can also be suppressed by the beat method described above.

Tracking simulation

We made simulation calculations for the first compressor. We have assumed that the loss parameter for the fundamental mode is 4.8 V/pC/m/ scaled from S-band structures. The bunch shape in DR was assumed to be Gaussian. Fig. 4.33(a) shows a phase space plot at the

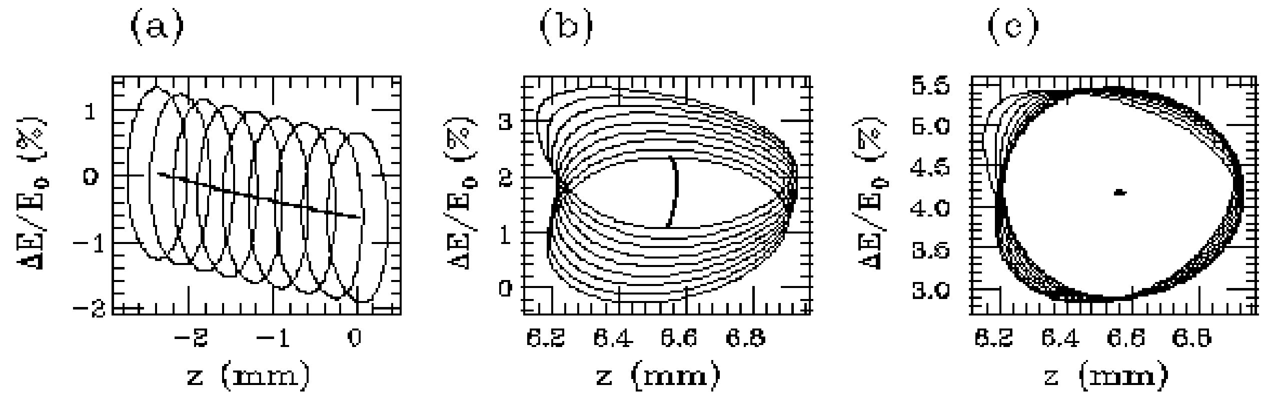

Figure 4.33: Phase space ellipses corresponding to 1σ beam ellipse. (a) without compensation. (b) with compensation. (c) with full-compensation.

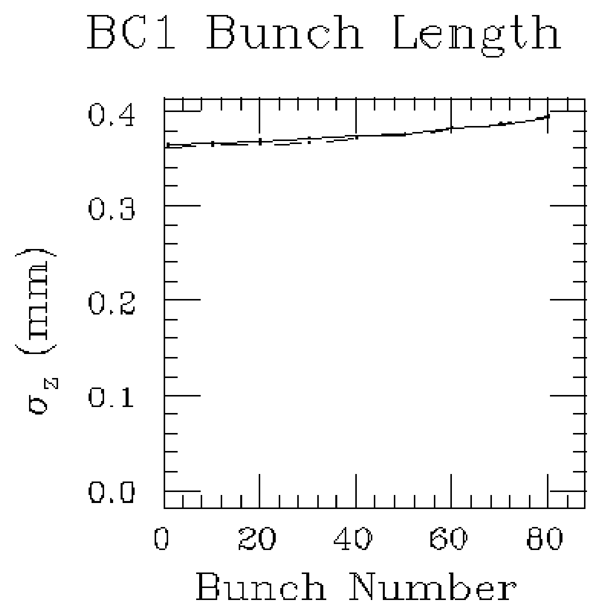

Figure 4.34: Bunch length dependence on bunch number.

end of the arc for the 1σ ellipse without compensation. It shows that the position shift in DR is converted to an energy shift and that the energy loss in the compressor cavity results in a position shift. Fig. 4.33(b) is the same plot but with energy compensation. A small position shift ($\sim 0.1\sigma$) is still observed due to a nonlinearity arising from RF sine wave of the main and the compensation cavities. Fig. 4.33(c) shows the results for the full compensation which includes the energy compensation at the end of the arc. The ellipses in the phase space are significantly deformed due to nonlinearities especially for the first and last bunch which are placed far off zero-cross phase of the main RF voltage. In the compensation cavity at the end of the arc we used an S-band structure because the position shifts are already corrected and, therefore, the nonlinear effect is expected to be small.

The bunch length is plotted versus the bunch number in Fig. 4.34. The solid line shows the rms bunch length fitted with Gaussian distribution using all particles and the broken line the rms value of particles within $\pm 3\sigma$ (fitted sigma) only. We find the bunch length varies by about 10 % from the head to the tail of a train.

4.5 0.3–0.5 TeV X-band Linac System

The essential advantage of the X-band over lower frequencies is that one can go to higher energies within a given length of the site. Since, however, the main target in this report is a relatively low energy, we will present here an X-band design with an accelerating gradient lower than that we had been planning for the last several years. This low gradient is believed to be feasible in the near future.

A possible RF system is shown in Fig. 4.35 to visualize the X-band system. This system is

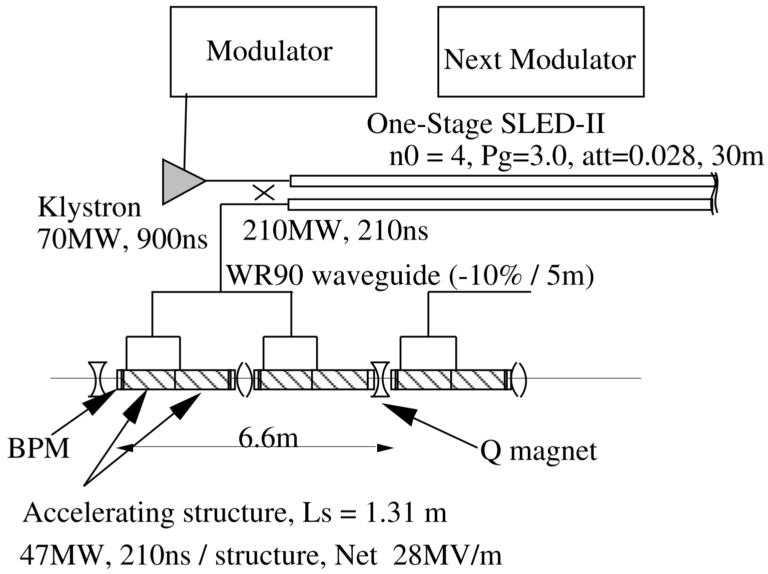

Figure 4.35: A schematic diagram of possible X-band RF acceleration system.

based on the following choice:

1. nominal (unloaded) accelerating field of 40 MV/m,

2. a klystron to power four accelerating structures,

3. one stage SLED-II with the net power gain of three (efficiency 70%),

4. waveguide loss of 5% (assuming 5m long rectangular waveguide).

5. use of 150-cell detuned accelerating structures with a/λ=0.18.

The accelerating structure and the beam dynamics will be described in the next subsection and the RF source in Sec.4.5.2.

4.5.1 Design of X-band linac

Design circumferences

The main linac should accelerate number of bunches in a train to the final energy without causing large energy spread nor emittance growth in a single bunch and in a multi-bunch sense. The relevant parameters from Yokoya[34] as of June 1992 are listed in Table.4.12.

Table 4.12: Beam parameters

Center of mass energy	$\sqrt{s}$	300	500	GeV
Final beam energy	E_f	150	250	GeV
Injection energy	E_{inj}	10	10	GeV
Number of particles / bunch	N	0.70	0.69	10^{10}
Bunch length	σ_z	85	67	mm
Bunch spacing	t_b	1.4	1.4	ns
Number of bunches / train	m_b	90	90	
Normalized emittance	ϵ_y	3×10^{-8}	3×10^{-8}	rad m

In the following discussion, we assume that the betatron amplitude function β in the linac varies as

$$\beta = \beta_1\sqrt{\frac{E}{E_1}} \tag{4.20}$$

where $\beta_1 = 3$ m at $E_1 = E_{inj} = 10$ GeV, giving the total phase advance φ through the linac as

$$\varphi = \frac{2\sqrt{E_1}}{\beta_1(dE/ds)}(\sqrt{E} - \sqrt{E_1}). \tag{4.21}$$

In this paper, we assume an optic based on the ordinary FODO structure with the phase advance of 90° per cell. Quadrupole magnets with the field gradient of 100 T/m can be used since the beam hole radius is less than 8mm. Then, they occupy 8.5% of the total length of the linac and the accelerating structures about 90%. This situation is listed in Table.4.13. The net accelerating gradient in the structure with the beam loading is about 28 MV/m. Then the average accelerating gradient dE/ds becomes 25 MV/m.

Table 4.13: Main linac parameters

Final beam energy	E_f	150	250	GeV
Total length of a linac		5.95	9.92	km
Phase advance / linac	φ	760	1058	radian
Number of quadrupole magnets		968	1347	

A group of several magnets and accelerating structures are aligned on some kind of a girder and pre-aligned by optical equipment. Then each girder will be aligned by using the beam and beam monitors. The alignment tolerances depend on the tuning strategy and the feedback method and should be studied in future.

The design of the accelerating structure is closely related to the beam emittance preservation and the needed RF power or wall plug power. Therefore, this design is one of the key issues for the main linac and are discussed in the following.

Single bunch transverse emittance growth

Single bunch emittance growth due to a random misalignment X_{rms} of cavities with respect to the beam is estimated as[34]

$$\frac{\langle x^2 \rangle}{\sigma_x^2} = \frac{0.218 L_s \beta_f \left\{ eN W_T'(0)\, \sigma_z \right\}^2}{(dE/ds)\epsilon_x (mc^2/e)} X_{rms}^2 \tag{4.22}$$

where L_s is the structure length and m the electron rest mass. It should be noted that the slope of the transverse wake field $W_T'(0)$ scales as $(a/\lambda)^{3.5}$ and the value used here is[34]

$$W_T'(0) = 1.4 \times 10^{20} [V/C/m^3] \quad \text{at} \quad a/\lambda = 0.16. \tag{4.23}$$

(A larger value of a/λ=0.18 is adopted in the general parameter list in Sec.4.1 to match the requirements at the low gradient in this report. Here, however, we shall use the old value 0.16 since most studies have been done with this aperture.)

The value of X_{rms} is determined by the accuracy of the cavity fabrication and the beam position monitor. It is believed to be better than 10μm. For L_s = 1.3 m, E_f = 250GeV, X_{rms} = 10 μm, and $\epsilon_x = 3 \times 10^{-8}$, the above formula gives the emittance growth

$$\frac{\delta \epsilon_x}{\epsilon_x} = \frac{\langle x^2 \rangle}{\sigma_x^2} = 0.14. \tag{4.24}$$

Multi-bunch emittance growth due to cavity misalignment

The multi-bunch emittance growth $\delta\epsilon$ (normalized emittance) due to the long-range deflecting mode with a low Q value is estimated as[34]

$$\delta\epsilon = \frac{4A^2 L_s \gamma_1 \sqrt{E_f E_1}}{\beta_1^3 (dE/ds)} X_{rms}^2, \tag{4.25}$$

with

$$A = A_0 \exp(-\frac{\omega_1 t_b}{2Q_1}) \quad \text{and} \quad A_0 = \frac{\beta_1^2 (eN) W_0}{2(E_1/e)}, \tag{4.26}$$

where ω_1, Q_1, and W_0 are the frequency, the Q-value, and the amplitude (per unit structure length) of the deflecting wake field. Let us consider the most severe transverse mode, TM110-like mode, at $\omega_1/2\pi \sim 1.5 \times 11.424$ GHz. Its W_0 is estimated to be roughly[35]

$$W_0 = 1.0 \times 10^{17} \left[V/C/m^2 \right]. \tag{4.27}$$

In this case,

$$A = 0.050 \exp(-75/Q_1). \tag{4.28}$$

If the emittance growth $\delta\epsilon/\epsilon_0$ should be less than 10% when X_{rms} = 10μm, the Q value for the deflecting mode should be less than 24. The above estimation was performed assuming that the excited wake field can perturb only the next bunch. This assumption will have to be checked by detailed simulations for individual designs.

Multi-bunch emittance growth due to injection error

The emittance growth due to the long range wake field in the presence of an injection error is examined. When $A\varphi < 1$, the second bunch is most affected, with the oscillation being given by[34]

$$X_2 = X_0\sqrt{1+(A\varphi)^2}\cos(\varphi - \arctan(A\varphi)), \tag{4.29}$$

where X_0 is the injection error of the first bunch. In order to suppress the emittance growth below 10%, $A\varphi$ should satisfy

$$\sqrt{1+(A\varphi)^2} < 1.05 \quad \text{or} \quad A\varphi < 0.32. \tag{4.30}$$

The Q value for the dominant TM110-like mode should be below 15 to meet this requirement.

Structure design

<u>(1) Damped structure</u>

In order to meet this low Q requirement, a damped structure was studied which has four damping waveguides in every cell[36]. Two of the damping ports are aligned in a line. The two lines are perpendicular to each other and one of them is positioned to border a disk in a cell while another to the disk in opposite side of a cell. To realize the Q value of the TM110 mode less than 15, the iris aperture of the damping waveguide should be larger than 9mm as shown in Fig. 4.36(a). Here, the height of the damping port was fixed at 2mm. Though the TE111-like mode seems to have a high Q value, its r/Q is smaller than that of TM110 by a factor of 100[37]. This factor is comparable to the damping of TM110 with $Q_1 = 15$ during the bunch interval. Therefore, a careful study for the actual design is needed. The Q value of this mode, however, must be much smaller than that of the pure TE111-π mode, since the mode is a mixture of TE111-like and TM110-like modes, the latter having a very small Q value. Other higher modes are well damped. In this design with 2mm iris width and 2mm damping port height, the Q and the r/Q of the accelerating mode are degraded by 16% and 4%, respectively, compared with the structure without damping port as shown in Fig. 4.36(b). There still remains a possibility to optimize the height of the damping port to obtain a little larger Q value of the accelerating mode.

Since the group velocity changes little by this type of damping waveguide, a structure with $a/\lambda = 0.16$ and $\tau = 0.69$ can be designed as follows. In Table.4.14 compared are the parameters of the structures with damping ports, "Damped", and that without, "Normal", for the unloaded gradient

$$\overline{G} = \sqrt{2\alpha r P_0}\frac{1-e^{-\tau}}{\tau} = 40\mathrm{MV/m}. \tag{4.31}$$

The Q and the r/Q values are estimated using SUPERFISH and the degradation from the normal disk-loaded structure is calculated by the 3-dimensional code MAFIA. Since the degradation of r/Q of the damped structure is only four percent, the required peak power is roughly equal for both the damped and normal structures with the same total attenuation parameter. However, the low Q value of the damped structure makes the structure length 16% shorter than the normal disk-loaded structure. Therefore, the length of a linac should be 16% longer, resulting in the increase of the number of the structures and the power sources by the same amount.

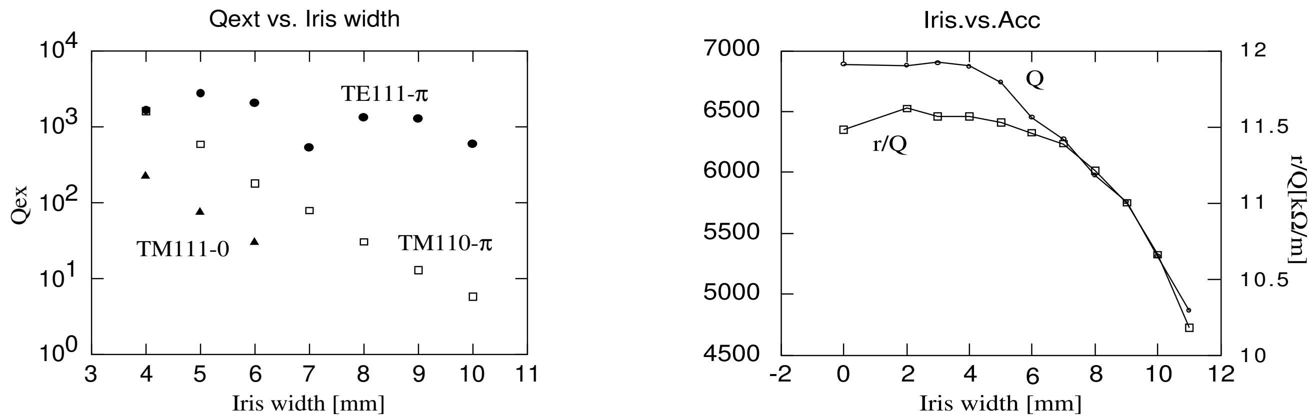

(a) (b)

Figure 4.36: (a) External Q values of three important modes to be damped and (b) the Q and r/Q values of the accelerating mode as functions of iris aperture width.

(2) Detuned structure

The Q and r/Q of the accelerating mode in the damped structure decreases due to a large damping hole in the cavity wall. If one can design a structure without holes such that the excited wake fields in all of the cells cancell each other at the arrival time of the following bunches, this degradation will be small while keeping the emittance growth small enough. Following this idea, a detuned structure [38, 39, 40, 41, 42] was examined. Consider a cavity with its transverse mode frequencies of the cells distributed over the range $\Delta f = 1/t_b$ and with the relative frequency difference $(f_i - f_{i+1}) = 1/(N_b t_b)$ between adjacent cells. Then the resultant wake field of the whole structure will be damped at t_b and the cancellation will continue till $N_b t_b$. As shown in the following example, the wake fields of the most severe transverse mode, TM110-like, were shown to be cancelled out below 1% over the period of a bunch train by properly distributing the mode frequency of the cells. In this example, the TM110 mode frequency of each cell in a structure of 150 cells is distributed according to a truncated Gaussian with the standard deviation $\sigma_f/f = 2.4\%$ and the full width $\Delta f/f = 12.5\%$. The wake field of such a structure is shown in Fig. 4.37(a), and the sum of the wake fields of four such kind of structures but with slightly different frequencies is shown in Fig. 4.37(b). The latter scheme is needed for a long bunch train more than 100 ns.

The accelerating field pattern of this structure is shown in Fig. 4.38. The average a/λ weighted by the dependence of the slope of transverse short range wake field $(a/\lambda)^{3.5}$ is set to 0.16. The sharp dip and peak near input and output coupler region is due to the Gaussian tail and can be compensated for by changing for example the disk thickness. The field in the figure corresponds to the input power $P_0 = 274$ MW and the average field 114 MV/m. The parameters to realize the unloaded gradient of 40 MV/m are listed in Table.4.14.

The above design is only an example and it still remains to optimize the number of cells in a structure to obtain better characteristics of the accelerating mode. The value a/λ may have to be a little larger to relax the alignment tolerance and the single-bunch beam loading. If we adopt 0.18 as in Sec.4.1, the required power will be 47 MW/structure as described in Fig. 4.35.

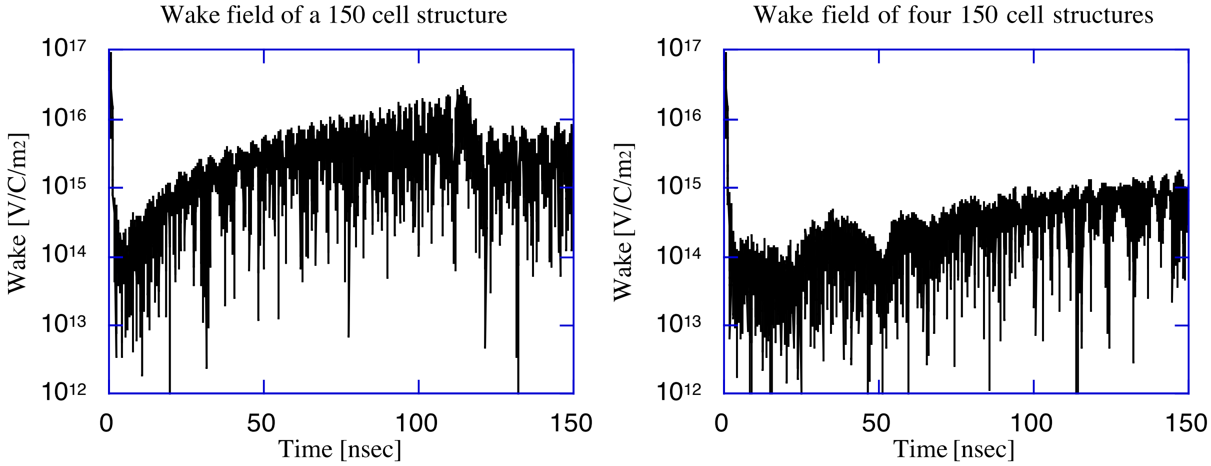

(a) (b)

Figure 4.37: Examples of the wake field of a detuned structure with 150 cells. (a) Wake field of a structure, (b) that of sum of four structures with slightly different frequency distribution.

Table 4.14: Parameters of the accelerating mode of a normal, damped and detuned structures with total attenuation parameter $\tau = 0.69$.

Parameters	unit	Normal	Damped	Detuned
type		CZ	CZ	
$\langle a/\lambda \rangle$		0.16	0.16	0.16
a	[mm]	4.20	4.20	3.14–5.40
τ		0.69	0.69	0.69
Q		6657	5592	6737–6545
r/Q	[kΩ/m]	12.23	11.74	9.44–15.4
r	[MΩ/m]	81.4	65.7	63.6–101
$\alpha = \omega/2v_gQ$	[m^{-1}]	0.471	0.561	0.204–1.316
L_s	[m]	1.47	1.23	1.31
Number of cells		167	141	150
P_0	[MW]	40.0	41.6	33.7
P_0/L_s	[MW/m]	27.3	33.8	25.8
T_f	[ns]	128	108	127
$T_f + N_bt_b$	[ns]	257	236	252

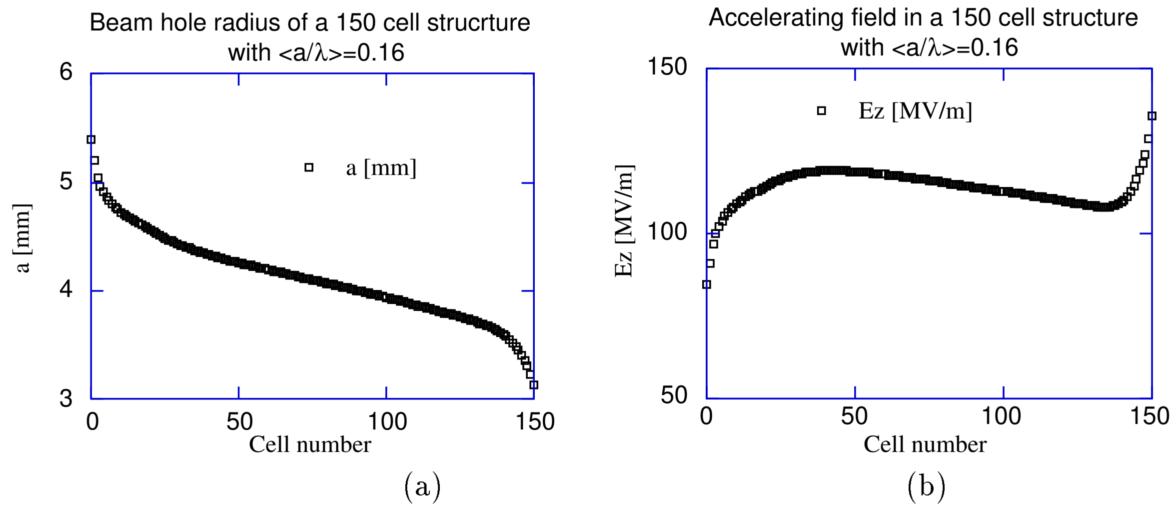

Figure 4.38: Beam hole aperture and accelerating field along a detuned structure with 150 cells.

Experimental R&D status

Controlling the frequency of transverse mode is very important in suppressing the emittance growth due to the long-range wake field. The precision of the frequency control for the detuned structure, for example, should be of the order of 10^{-4}. Since the needed accuracy for the accelerating mode is around 3×10^{-5} to make the total phase shift along the structure with 100 cells below 2 degrees, the fabrication of the structure without tuning has been studied. If this tuningless structure can be made, the frequency of the dipole mode is automatically well controlled. To this aim, the precise fabrication techniques are studied such as ultra-precision machining, fine brazing, diffusion bonding, and so on. A precise fabrication of a 20-cell brazed structure should be tested in a few months.

A high gradient experiment for a 20 cm long structure which was fabricated in the ordinary manner by a company is underway. After 500 hours' conditioning, a gradient of 70 MV/m level was achieved. A further conditioning seems rather difficult due to frequent RF breakdown. Significant amount of field emission current of the order of mA was observed. However, the operation at the gradient of 40 MV/m level seems easy to realize. At this level, the field emission current is as low as μA and may not cause severe problem. This low dark current is also explained by a simulation code[43] which shows a critical gradient of 80 MV/m below which any field-emitted electrons cannot be trapped in RF phase to be accelerated to higher energies along the structure.

The requirement on the vacuum in the linac is around 10^{-8} Torr to prevent beam halo due to the beam-gas scattering which causes background problem in the final focus region. The vacuum level in the present experiment is estimated to be 10^{-7} Torr or worse. The structure was evacuated by four 20 liter/sec ion pumps through two coupler irises with 5×7.5 mm^2 opening and two beam pipes at both ends of the structure with the diameter 6 mm and length 1 cm. In a realistic design, more efficient pumping should be needed.

Summary and future program

Two kinds of possible X-band accelerating structures were described. A peak power of 35 to 45 MW with pulse length of 240 to 260 nsec is needed for the accelerating field of 40 MV/m level, which is equivalent to the net accelerating field of 30 MV/m after performing the single- and multi-bunch beam loading compensation.

Engineering R&D for precision fabrication of a detuned structure or a proof of fabrication of a damped structure should be performed soon.

4.5.2 X-band RF System

Introduction

In the R&D program started in 1988 for X-band klystrons, two types of klystrons have been designed and tested[44]. The first one is a 30 MW class klystron named XB-50K. This rather moderate peak power klystron was designed as the first step to the 100 MW class klystron and produced 18 MW peak power. It supplied the RF power to the first X-band accelerating structure test in 1992.

The second klystron named XB72K was designed as the first 100 MW class klystron which could possibly satisfy the minimum power requirement as the RF power source for an X-band linear collider of several hundred GeV per beam. The first XB-72K was tested in 1992 spring and summer. Its result is also reported here.

XB-50 Series

XB-50K's are 30-MW class klystrons developed as the first step toward 100-MW or higher. Design parameters are summarized in Table 4.15. The main purpose of this rather moderate peak power klystron is firstly to produce RF-power useful for high-power tests of X-band RF parts including the accelerating structures.

Table 4.15: Design Specifications (XB-50K)

Operating Frequency	11.424 GHz
Peak Output Power	30 MW
RF Pulse Width	$\sim$ 500 nsec
Pulse Repetition Rate	50 $\sim$ 100 pps
Beam Voltage	420 kV
Beam Current	160 A
Efficiency	45%
Saturated Gain	53 dB
Focusing Field	4.6 kG
Beam Areal Compression	80:1
Max. Surface Grad. in Gun	260 kV/cm
Max. Surface Grad.	1000 kV/cm
Average Cathode Current Density	7.8 A/cm^2

Prior to the klystron construction, a test diode named XB-50D was fabricated and tested in 1989[45], and reached the cathode voltage of 480 kV. After this diode test, the final design of the XB-50K shown in Table 4.15 was decided, and three XB-50K's have been already completed. The first of them has been tested twice with some modification in the ceramic window[46]. By now XB-50K has been tested up to the RF-power of 18 MW with the pulse duration of 100 ns, and successfully operated for 500 hours up to 18 MW as the power source of the first high gradient test for X-band accelerating structures[47].

Following are the summaries of these tests of XB-50D(test diode) and XB-50K(30 MW class klystron).

XB-50D

1) Design and fabrication XB-50D is a Pierce type electron gun designed for the test of high voltage pulsed electron gun as the beam source of the XB-50K klystrons. The purposes of this tube are 1) to produce the beam power of 80 MW or more, necessary for the RF output power of 30MW, assuming the RF conversion efficiency of 40%, 2) to check the limit of high voltage breakdown in the gun structure, especially in the cathode ceramic part, and 3) to test the new Ir-coated dispencer cathode[49]. As a cathode ceramics, the cylindrical ceramics supplied by WESGO for SLAC #5045 klystrons was selected because of the successful results in the SLC operation.

The design parameters are summarized in Table 4.16. The gun simulation was done using E-GUN code written by W.B.Herrmannsfeldt[48]. To test the high voltage limit in the gun region, the maximum surface field was designed to be high, compared to the present S-band high power klystrons such as #5045 and E-3712. The surface field distribution around the cathode and the anode was calculated by "DENKAI" written by T.Shintake. Over 300 kV/cm surface field strength could be tested at rather low cathode voltages of less than 300 kV. The cathode radius and perveance were determined so as to keep the beam areal compression ratio at 80 to 1 (see Table 4.15), in order to make the focusing relatively easy.

Table 4.16: XB-50D parameters

Cathode Voltage	380 kV	(450 kV)
Beam Current	130 A	(170 A)
Beam Power	50 MW	(80 MW)
Maximum Surface Field	310 kV/cm	(365 kV/cm)
Perveance	0.57 micro-perveance	
Cathode Diameter	50 mm	
Cathode Spherical Radius	60 mm	
Cathode Material	Ir-coated dispenser cathode	

The fabrication of the XB-50K was carried out by TOSHIBA Corporation with the ordinary fabrication method of high power pulsed klystrons. The first XB-50K was delivered to KEK in 1989 spring.

2) Test results The high voltage operation test was carried out from 1989 autumn to 1990 spring. To drive XB-50D, a modulator originally designed for #5045 was modified to adjust the pulse length of the PFN by reducing the number of stages down to 3. Also, the impedance of the PFN was adjusted to that of the test diode tube. After a short period of spot-knocking, i.e., the high voltage operation without cathode emission, the high voltage processing started from the cathode voltage of 200 kV. The maximum cathode voltage achieved after 70 hours of conditioning mostly at 2 pps was 480 kV with the pulse half width of about 3 μsec. No serious discharge was observed until this voltage was achieved. At 430 kV a reasonably stable operation was sustained at the repetition rate of 100 pps, where the fault rate was once in 10^5 pulses. A stable operation around 400 kV or slightly higher could be expected for this gun structure with this cathode ceramics.

XB-50K

1) Design and fabrication XB-50K is the first X-band klystron in the R&D program for the future linear collider in Japan. As the first step to the final power source, a rather conservative target of 30MW output power was chosen, since an actual power source was needed for various high-power tests in X-band linac technologies.

The cathode structure of this tube was almost the same as XB-50D with only a slight change applied to the wehnelt and anode geometry for the purpose of relaxing the surface stress without sacrificing the focusing characteristics. At the cathode voltage of 450 kV, the maximum surface stress was reduced to 260 kV/cm from the value of 365 kV/cm in XB-50D. The RF simulations were performed using FCI-code written by T.Shintake[50], and the final design parameters are summarized in Table 4.15.

One of the important parts in a high power pulsed klystron is the ceramic window. The #1 tube had a half-wavelength ceramic-type window. At the first high power test, however, it was broken due to an RF discharge, which will be described later, and was replaced with a new pillbox type window. XB-50K#1a (the repaired one after the failure) and the following XB-50K's have such windows, of which dimensions are shown in Fig. 4.39.

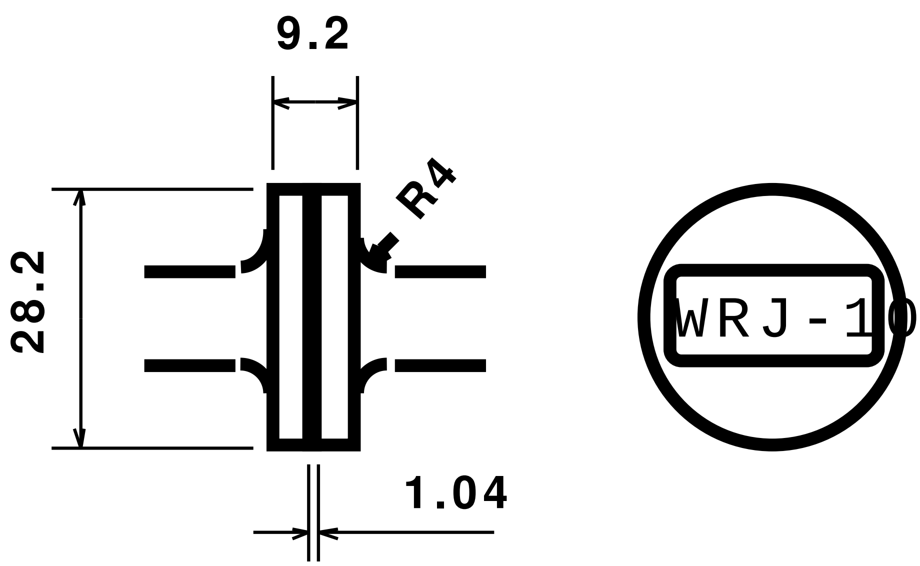

Figure 4.39: Output Window Dimensions of XB72K & XB50K Klystron

By June 1992, #1,#1a,#2, and #3 XB-50K's were delivered to KEK. Among these, #1 and #1a were already tested and #1a has been operated as the RF power source for the X-band accelerating structure test. All of these XB-50K's were fabricated by TOSHIBA Corporation.

2) Test results XB-50K#1 was tested up to 11 MW peak power in 1990, and XB-50K#1a up to 18 MW with the pulse duration of 100 ns. Results of these tests are shown in Fig. 4.40 and the experimental set up in Fig.4.41.

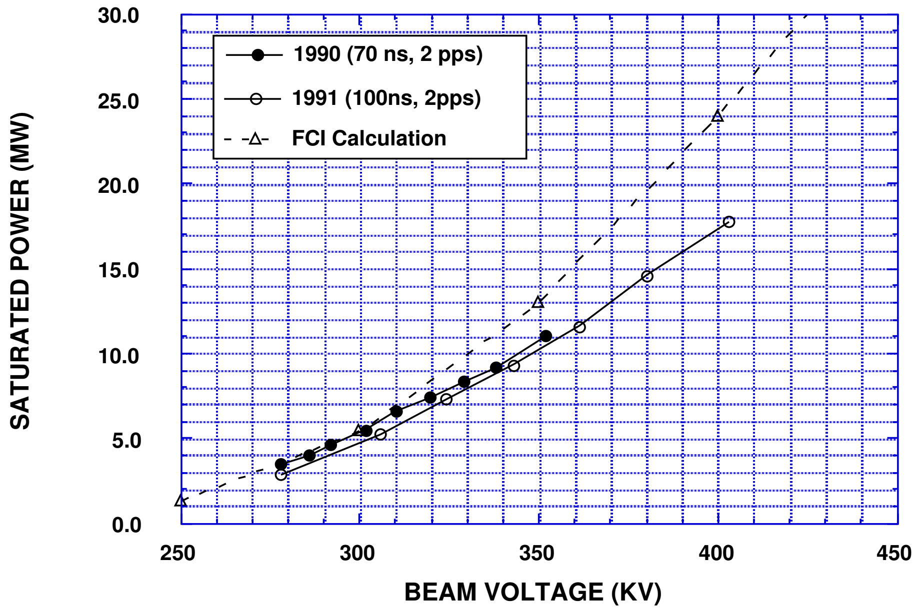

Figure 4.40: XB50K Saturated power.

The half-wavelength type window of XB-50K#1 was broken at the peak power of 11 MW with the pulse duration of 70 ns. This failure was identified as due to a hard RF discharge on the ceramic surface. A serious damage was observed on the atmospheric side of the window. There was an air leak through the ceramics, which is fatal for the vacuum tube. Discharge marks of the sputtered metal film was observed on the ceramic surface and fine powder of chipped ceramics was found inside the wave guide. The damage was harder outside the tube than inside. This was possibly due to the fact that the vacuum pressure in the guide was higher, because no bakeout process was applied to the waveguide vacuum system.

In 1991 summer, XB-50K#1a was tested up to 18 MW with the pulse duration of 100 ns. Up to this power and pulse length, the new pill-box window exhibited only slight discharge and no damage was observed. This same tube was again operated in 1992 spring as the power source for the high gradient test of the 20 cm X-band structure. From April to June, it supplied the RF power up to 16$\sim$17 MW with 50nsec at 2$\sim$100 pps for 500 hours.

As shown in Fig. 4.40, the measured efficiency at 18MW was still less than the FCI simulation value by 30%. Similar discrepancies have also been seen at SLAC and VLEPP, although the klystrons were designed based on different simulations. The problem might be related to the beam focusing and interception since the drift tube radius is much smaller than in the established S-band klystrons. It is planned as a next step to survey the magnetic field on and near the cathode surface. Also to be analyzed in more detail are the gun design and the beam characteristics around the output cavity, especially at its downstream end.

In Fig. 4.41, the XB-50K#1 and its experimental set-up for high power test are shown.

At the present stage of XB-50K klystrons, the following results have been obtained.

(1) 50-100nsec, 18 MW RF power was obtained and utilized for the X-band acceleration structure test. After 500 hours of operation dedicated to the test at 2 to 100 pps, XB-50K#1a

Paste a picture here.

Figure 4.41: Experimental setup for XB50K.

has not shown any degradation in its performance.

(2) RF efficiency was measured as ~30% at the peak power of 18 MW and was lower than the simulation result of 42%.

(3) Diode characteristics, such as cathode voltage, perveance, beam current, and fault rate, are in good agreement with the designed values.

(4) The ceramics window of pill box type had only a slight discharge without damage. For the longer pulse required for the linear collider, further improvements will be needed.

XB-72K Series

XB-72K is the 100-MW class klystron designed as the prototype which satisfies the minimum peak power requirements for the future X-band linear collider. The main goal of this klystron is to produce the peak RF power of 100 MW or higher. With a help of some RF pulse compression scheme, this klystron can produce the peak RF power of 400 MW. Some problems such as the low modulator efficiency and the power-consuming focusing magnet are left open for future studies.

XB-72K

1) Design and fabrication The necessary beam power is more than 250 MW if one assumes the RF efficiency of 40%. Considering the present state of the art in the pulsed high-power klystrons, the cathode voltage of 550kV was chosen as the first step. This voltage is about 30 % higher than that of the existing high-power klystrons such as #5045 or other S-band fleet widely used in the present S-band linacs. The flat top length needed for our klystron with the 4-times pulse compression system will be around 500 nsec which is much shorter than the S-band ones above. Therefore, the cathode voltage of 550 kV to 600 kV is believed to be within the reach of the present high voltage pulse technology. By the use of E-GUN code the diode design of the XB-72k was carried out and the final design parameters are summarized in Table 4.17.

Table 4.17: Design Specifications(XB72K)

Operating Frequency	11.424 GHz
Peak Output Power	120 MW
RF Pulse Width	$\sim$ 500 nsec
Pulse Repetition Rate	50 $\sim$ 100 pps
Beam Voltage	550 kV
Beam Current	490 A
Efficiency	45%
Saturated Gain	53 $\sim$ 56 dB
Focusing Field	6.5 kG
Beam Areal Compression	110:1
Max. Cathode Current Density	17 A/cm^2
Max. Surface Grad. in Gun	273 kV/cm
Max. Surface Grad. in Output Gap	720 kV/cm

Considering the drift tube radius and the cathode size which is limited by the maximum available current density, the beam areal compression ratio was chosen as 110 and the perveance as 1.2 micro-perveance. This perveance is considered to be the best compromise between the easy beam focusing and the low impedance for the fast rise time of the cathode voltage wave form which is definitely important for the power supply efficiency. Simulations by E-GUN code showed that a good laminar flow can be obtained in the drift tube region with the focusing field of 6.5 kG. The designed gun structure is shown in Fig. 4.42. The beam trajectory obtained by the E-GUN code is shown in Fig. 4.43. Although the cathode voltage is higher by $\sim$30% than that of XB-50K, the surface gradient in the gun structure is kept relatively low, 273 kV/cm at most. The maximum current density on the cathode is 17 A/cm^2. This is considered to be feasible from our operating experience of XB-50K which has the same Ir-coated dispencer cathode. Even at this current density, the cathode temperature is estimated to be 1050^{o}C or slightly lower, and the cathode life time longer than 10^5 hours can be expected at this temperature.

RF simulations were carried out by the use of the FCI code as in the case of XB-50K's. The cavity configuration from the input to the output cavities are shown in Fig. 4.44. The output and penultimate cavities are the so-called "noseless type cavities"[51]. Owing to them the

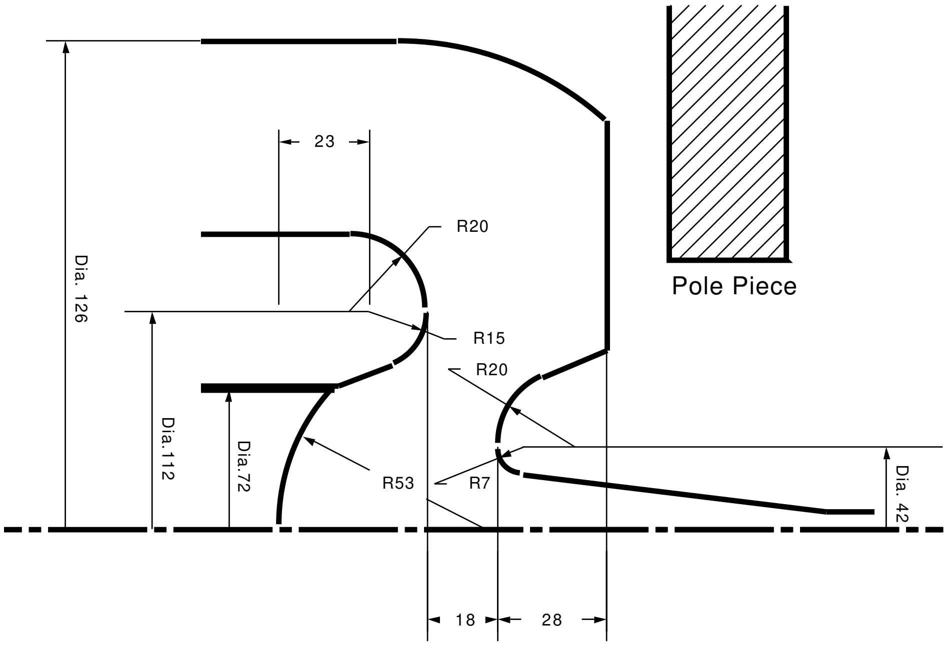

Figure 4.42: Gun dimensions of XB72K Klystron

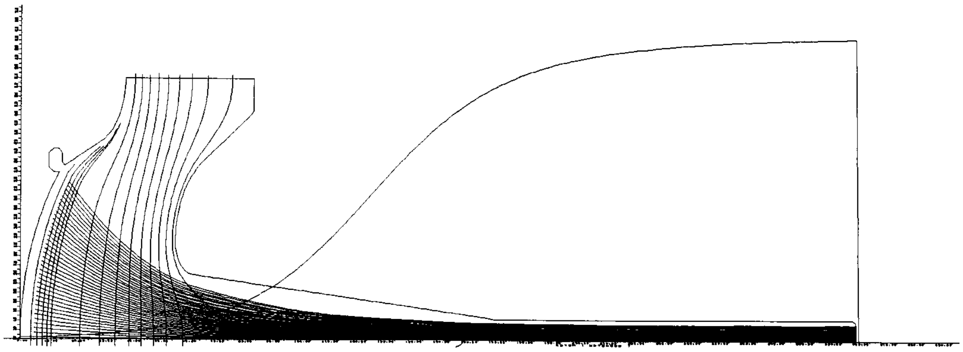

Figure 4.43: The beam trajectory in XB-72K simulated by E-GUN.

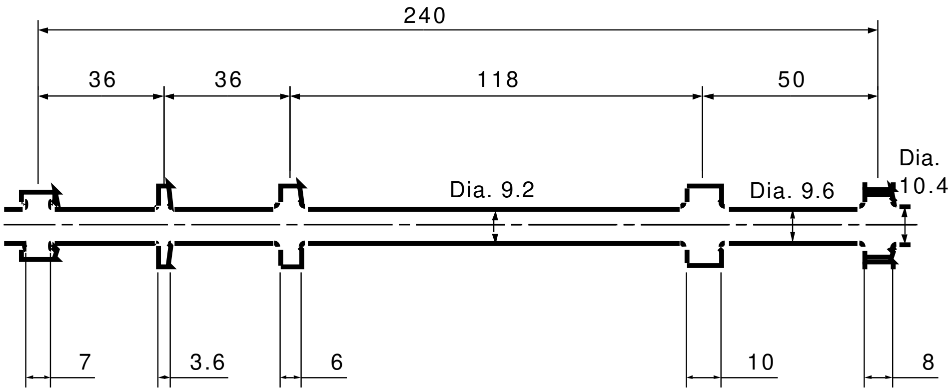

Figure 4.44: Interaction geometry of XB72K Klystron

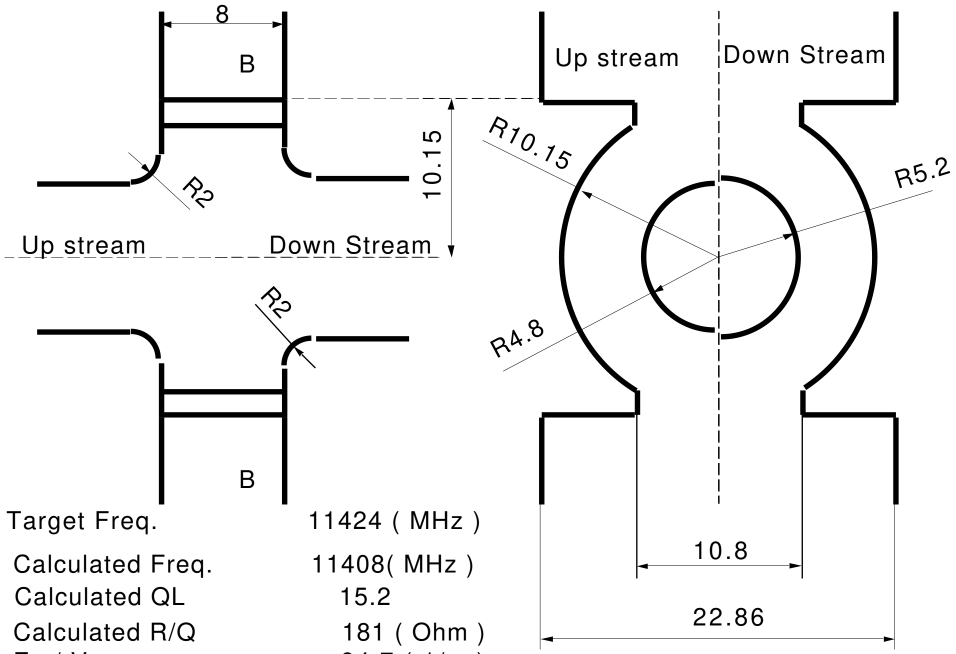

Target Freq.	11424 (MHz)
Calculated Freq.	11408(MHz)
Calculated QL	15.2
Calculated R/Q	181 (Ohm)
Es / Vc	84.7 (1/m)

Figure 4.45: Output gap dimensions of XB72K Klystron

maximum surface field in the output gap can be kept as low as 700 kV/cm in spite of the single output gap structure. The output cavity has two output waveguides attached symmetrically, and two pill-box type ceramic windows are set on each waveguide. These windows have the same structure as those in XB-50K's, which have worked up to the RF output of 18 MW with 100 nsec pulse duration.

2) XB-72K Test results The first XB-72K fabricated by TOHSHIBA was delivered to KEK in January 1992 and a test system with a new modulator were set up in the assembly hall in KEK site. The setup with the output waveguide system is shown in Fig. 4.46. For

Paste a picture here.

Figure 4.46: The test system for the first XB-72K tube.

the operation of XB-72K to higher cathode voltages than previous tubes, a concrete radiation shield was prepared. The two output windows are connected to individual matched loads and the output RF power was measured separately on each wave guide.

The first high power test of the XB-72K#1 was carried out last April. At the cathode voltage of 430 kV with the RF output power of 22 MW in 100 ns, the gun ceramics had a small but fatal air leak and the test was terminated[52]. After removing this gun ceramics, the inside wall of the drift tube section was examined by a fiber scope for medical use and no visible damage was found from the anode to the downstream end of the output cavity. Apparently, up to this cathode voltage and this RF output power, no serious beam interception did exist in the beam drift section.

XB-72K#1 was rebuilt with a new gun ceramics, cathode, and windows. The high power test was resumed from August 1992[53]. The high power characteristics obtained in these experiments are summarized in Figs. 4.47, 4.48, and 4.49. Fig. 4.47 shows the measured

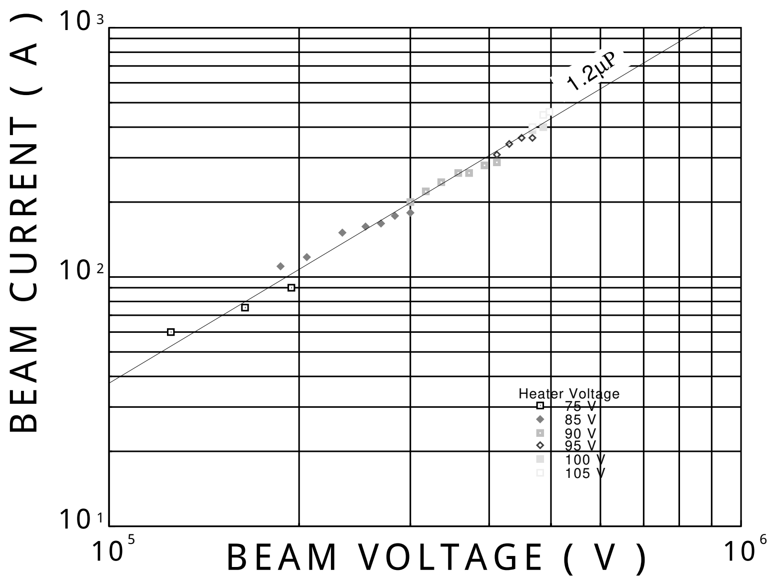

Figure 4.47: XB72K#1A Perveance curve.

perveance of the XB-72K#1a, which is in good agreement with the simulation result shown by the solid line. Fig. 4.48 shows the saturated RF power versus beam voltage. The RF output power reached 41 MW at the cathode voltage of 500 kV. Fig. 4.49 shows the RF conversion efficiency versus beam voltage. The measured efficiency is still lower than the simulation, on which further studies are needed.

The tentative results obtained in these XB-72K high power tests are as follows. This XB-72K#1a is still under conditioning toward higher cathode voltages.

(1) 500 kV beam voltage was achieved.

(2) 230 MW beam power was obtained.

(3) The measured perveance curve is in good agreement with the design value.

(4) RF output power of 41 MW was obtained. The RF efficiency was 18 %.

Modulator

1) Modulator for XB-72K The ordinary modulator which is currently used as the power supply for the XB-72K test cannot have the high power efficiency necessary for the future linear collider due to the rather long rise and fall times of the cathode driving pulse. The switching speed is mainly determined by the stray capacitance and inductance of the pulse transformer in the present modulator system. To shorten the rise and fall times and improve the modulator efficiency, raising the primary voltage thus relaxing the step-up ratio of the pulse transformer will be effective. The Blumlein type configuration of two PFN's can double the output voltage compared to the ordinary single stage PFN. This type of PFN has the advantage of introducing no new components such as a thyratron and a capacitor. A design of

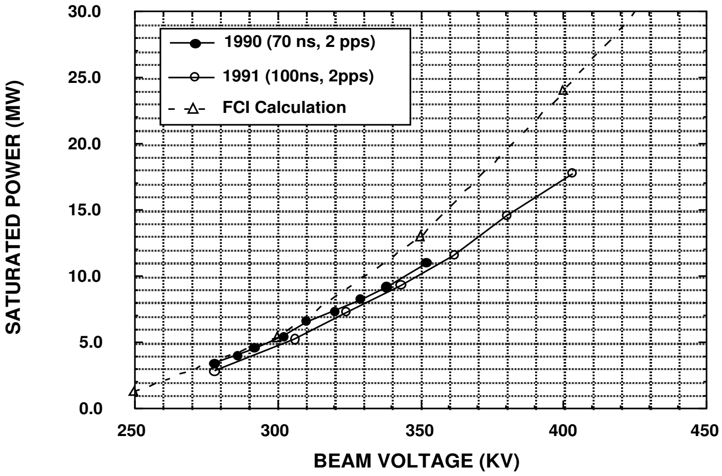

Figure 4.48: Saturated power of XB-72K#1.

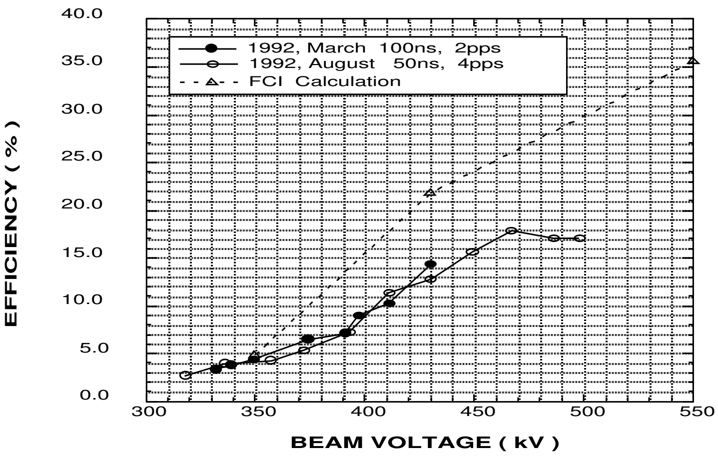

Figure 4.49: Efficiency of XB-72K#1.

this Blumlein type PFN has been completed and an operation test is scheduled in the end of 1992 FY. The design parameters are shown in Table 4.18. This system is expected to reach 80 % modulator efficiency.

Table 4.18: Modulators for X-band Klystron (XB-72K)

Design Parameters

(a) PFN (Blumlein Type)	
Rise Time (with Trans.)	$\sim$ 150 ns
Fall Time (with Trans.)	$\sim$ 230 ns
Flat Top	$\sim$ 500 ns
Number of PFN	8-stages + 8-stages
Output Voltage(=Charging V)	80 kV (1:7 Step-up)
Impedance	23 Ohm(XB-72K 550 kV)

(b) Pulse Trans. (Primary at 80 kV while charging)	
Step-up ratio	1:7
Leakage L	830 nH
Stray Capacitance	4 nF (Primary)
Loss at 200pps	100 W (Hysteresis)
	1000 W (Eddy Current)
Rise Time (Trans. only)	$\sim$ 100 ns
Fall Time (Trans. only)	$\sim$ 200 ns
Sag.	2.8% (after 500 ns)
Core Material	Si-Fe (t=25 micron)

PERSPECTIVES

The recent progress in the X-band RF power sources at KEK described above has shown that the minimum requirement for the linear colliders of the next generation can be satisfied by the X-band klystron system powered by the improved type of modulators. Within a few years, we expect to have a proto-type X-band klystron system with an RF power compression system which satisfy the minimum requirements such as the power efficiency, stability, peak power of 100 MW class and the pulse duration of 500 ns or longer. For this goal, further intensive R&D works including the development of the RF window, the modulator, and the RF power transfer system will be necessary.

4.6 0.3–0.5 TeV C-band Linac System

Since several years ago we have been developing an X-band RF system for JLC. Although it can potentially provide a high accelerating gradient, there are still a number of technical problems to be solved. With the S-band, on the other hand, the linac would be very large and long even for 0.5 TeV, albeit less R&D works would be required. In this section we discuss the possibility of an intermediate frequency range C-band, from which for definiteness we choose 5712 MHz, i.e., twice the SLAC frequency.

Expected advantages of the C-band scheme are as follows.

1. The RF pulse to be generaged by a klystron is a few μsec in length. Hence, a conventional HV pulse modulator will suffice. Only an engineering study will be required on the modulators to reduce the size and the cost.

2. The peak RF power to be generated by a klystron is less than 50 MW, and the high voltage applied to klystron is only 300 kV. These requirements are moderate and are expected to be met by a straightforward extension of the well-established S-band klystron technologies.

3. The RF pulse compression of the SLED-II type is feasible within a reasonable size by using delay lines of a disk-loaded structure.

For the accelerating structure, we adopt a recently proposed damped cavity which makes use of the radial line damper and the choke structure. With this cavity, multi-bunched beams can be accelerated without serious instabilities. Although this new type of cavity is not instrinsic to the C-band but can be applied to S- and X-band as well, we shall describe it in this section since it was proposed in the course of the design study of the C-band.

4.6.1 Outline of C-band Linac

The whole JLC complex should be accomodated in a site at most about 25km in length. If we take into account the length of the final focus system and the space for the linac focusing elements, the active structure length for each linac has to be about 8km. In order to reach 250 GeV within this length, the net accelerating gradient must be at least about 30 MeV/m. If we take into account the beam-loading and the single/multi-bunch energy compensation, a nominal gradient of 40 MeV/m is required. A crude optimization of the collider system is given in Sec.4.1. After some refinement, the basic parameters for the C-band linac are summarized in Table 4.19.

A schematic diagram of the one section of the RF system is shown in Fig.4.50. It consists of a HV pulse power supply (modulator), two klystron amplifiers, two SLED-II type pulse compressors, and four accelerating structures. This section is repeated at every 8.8 meters.

If one simply scales the conventional S-band SLAC structure down to the C-band, the length of a cavity unit becomes about one meter. A longer unit may be more economical because each needs input and output couplers, vacuum jackets, etc. On the other hand, the peak input power increases in proportion to the length, and also the iris radius needs to be larger to make the group velocity fast enough. Consequently, the shunt impedance becomes lower because the electric field concentrates on the disk edge, resulting in a lower ratio of the accelerating gradient to the stored RF power. We therefore choose 2m unit length as a compromise. The filling time is then about 300 nsec as seen in Table 4.19. Since the beam pulse length is 100 bunches $\times$ 2.8nsec = 280 nsec, the RF pulse length into the structure must be about 600 nsec. The required peak power per cavity unit is 85 MW. 3

This RF pulse (85MW$\times$0.6μsec) or each 2m structure will be provided in the following way. A HV pulse mudulator of conventional type creates an output voltage 302 kV with a flat top length of 3.6μsec. This power is fed into two klystrons, each of which produces an output RF pulse of 45MW$\times$3.6μsec. This long pulse is compressed to 0.6μsec by a SLED-II type

Table 4.19: C-band main linac parameters

Beam Parameter			
Frequency	f_{RF}	5712	MHz
Beam energy	E	250	GeV
Number of p 71 article per bunch	N	1×10^{10}	
Number of bunches per pulse	N_b	$80 \sim 100$	
Bunch spacing	t_b	2.8	nsec
Repetition frequency	f_r	150	Hz
Main Linac			
Nominal gradient	E_{a0}	40	MV/m
Net accelerating grad.	E_a	28.7	MV/m
Total active length per beam		8362	m
Accelerating Structure			
Cavity type	Damped cavity with choke		
Damped Q-value of TM_{110} mode		< 5	
Iris radius/wave length	a/λ	$0.16 \sim 0.12$	
Group velocity	v_g/c	$0.042 \sim 0.017$	
Attenuation parameter	τ	0.57	
Filling time	t_F	297	nsec
Q-factor	Q_0	7932	
Shunt impedance	r	$47 \sim 64$	MΩ/m
average	$\langle r \rangle$	55	MΩ/m
Peak RF power per structure		85	MW
Loss factor	k	67.8	V/pC/m
Single bunch loading	kq	0.11	MV/m
Multi bunch loading	$E_a - E_f$	8.0	MV/m

compressor. The efficiency is estimated to be 70% so that the peak power becomes 190MW. The output of each klystron drives two accelerating structures. Assuming a loss of 10% in the wave guide, we obtain the required pulse stated above. The pulse structure is depicted in Fig.4.51.

The detail of the klystron and the compressor will be described in the next subsection and the accelerating structure in Sec.4.6.3.

4.6.2 C-band RF-Source

The parameters of the C-band RF source are summarized in Table 4.20.

The C-band Klystron

Achievable RF power per klystron The maximum RF output energy from a klystron generally decreases with frequency. Because the drift tube cross-section in a klystron is inversely proportional to the RF frequency squared, so is the available power. Fig. 4.52 shows the pulse

Table 4.20: C-band RF-system

Klystron			
Klystron peak power	P_0	45	MW
Pulse length	t_{RF}	3.6	μ sec
Gun Voltage	V_0	302	KV
Gun perveance	K	2.0	$\mu A/V^{1.5}$
Beam current	I_0	331	A
Power efficiency	η	45	%
Pulse Compressor SLED-II			
Multiplication index	n	6	
Loss factor in delay line	τ	0.01	
Resistive power loss		10	%
Reflection power loss		20	%
Energy efficiency		70	%
Power gain	P_0/P_{in}	4.2	
HV Pulse Modulator			
HV Power		302kV× 331A	
Pulse rise and fall time		0.55 and 0.5	μsec
Pulse efficiency		80	%
Pulse energy	900	Joul	
Repetition frequency	f_r	150	Hz
Power consumption	P_{AC}	135	kVA
System Power Efficiency			
Modulator pulse efficiency		80	%
Klystron efficiency		45	%
Klystron focusing coil power		3kW (4.4)	%
Pulse compressor efficiency		70	%
Waveguide loss		10	%
Total power efficiency from AC from to RF input to the structure		22	%

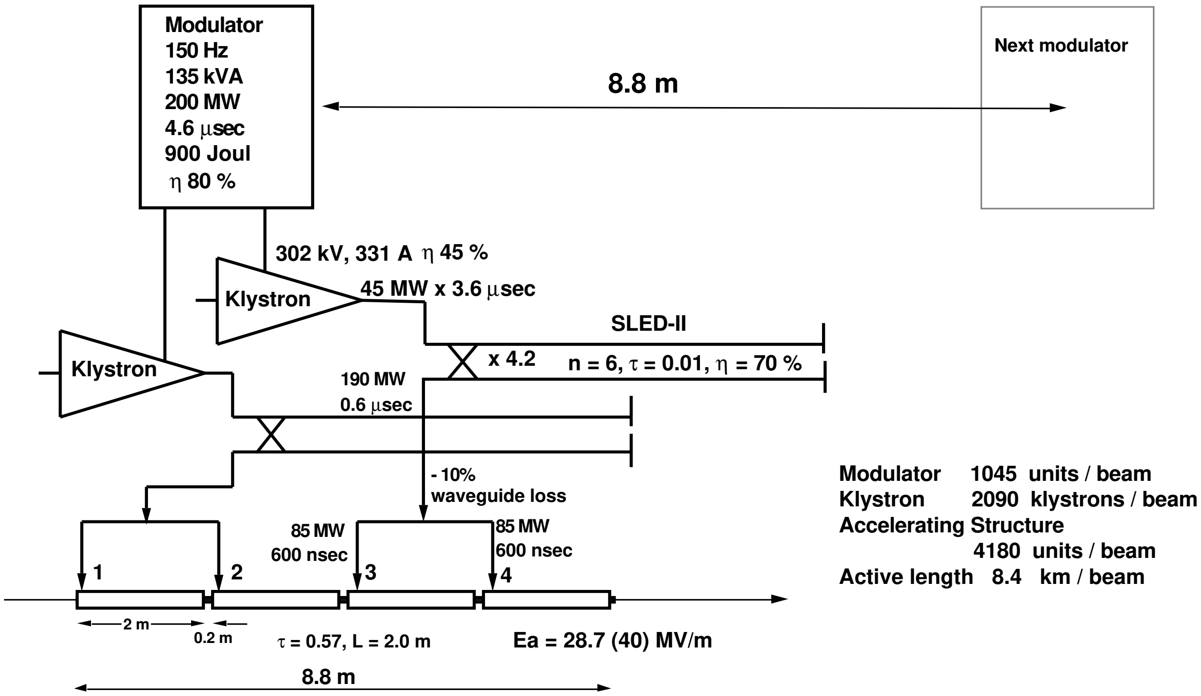

Figure 4.50: The RF system of the C-band main linac.

energy (peak power multiplied by pulse length) obtained from existing high power klystrons as a function of the operating frequency. All of them are pulsed klystrons used in linear accelerators. The data near 3 GHz are for the SLAC 5045 klystron developed at SLAC. More than 200 tubes of this type have been successfully operated in the SLC project. The data at 8 and 11 GHz are from R&D tubes developed also at SLAC for the NLC project. The 11 GHz klystron has recently generated 50 MW and 1 μsec pulse. These data seem to show $1/f^2$ dependence. The lower solid line is a theoretical limit derived under the assumption that the HV break down around the output cavity is initiated by meltdown of the copper drift tube due to collision of infinitely short drive beams. In practice, however, the thermal energy quickly diffuses into the tube body and the surface temperature decays in several tens of nanoseconds. Since the drive beam in klystron is gerenally much longer than this decay time, the surface temperature stays lower than in the impulse case. Therefore, actual tubes work better than the impulse theoretical limit.

The upper solid line shows our guesstimate on the practical limit. This limit for a few μsec pulse is

$$W_b \sim 1.3 \times 10^4/f^2 \qquad \text{(Joul/pulse)} \qquad (4.32)$$

where f is the RF frequency in GHz, and predicts approximately 400 Joul/pulse at 5.7GHz. Supposing 50% power efficiency from the drive beam power to the RF output, the available maximum RF energy becomes 200 Joul/pulse, corresponding to 56 MW in 3.6μsec, well above our design value of 45 MW.

Electron Gun and HV pulse Suppose the perveance of the electron gun of the C-band klystron to be $2\times10^{-6}A/V^{1.5}$, then the HV pulse to drive the klystron becomes 302 kV, and the feeder peak current 331 A. For the reliability of high power klystrons, one of the most important parameters is the gun voltage applied to the electron gun cathode. The 5045 klystron working

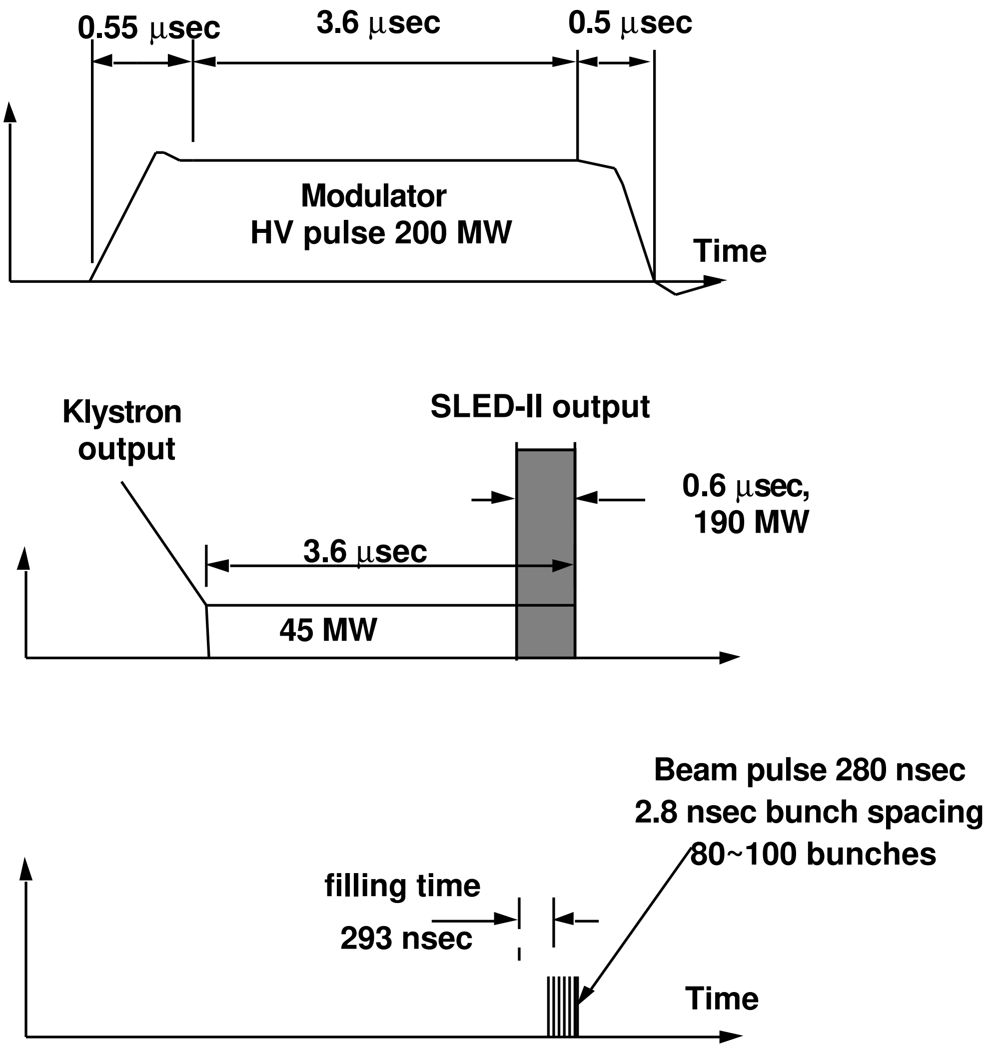

Figure 4.51: The Klystron and beam pulse structure for the JLC C-band linac.

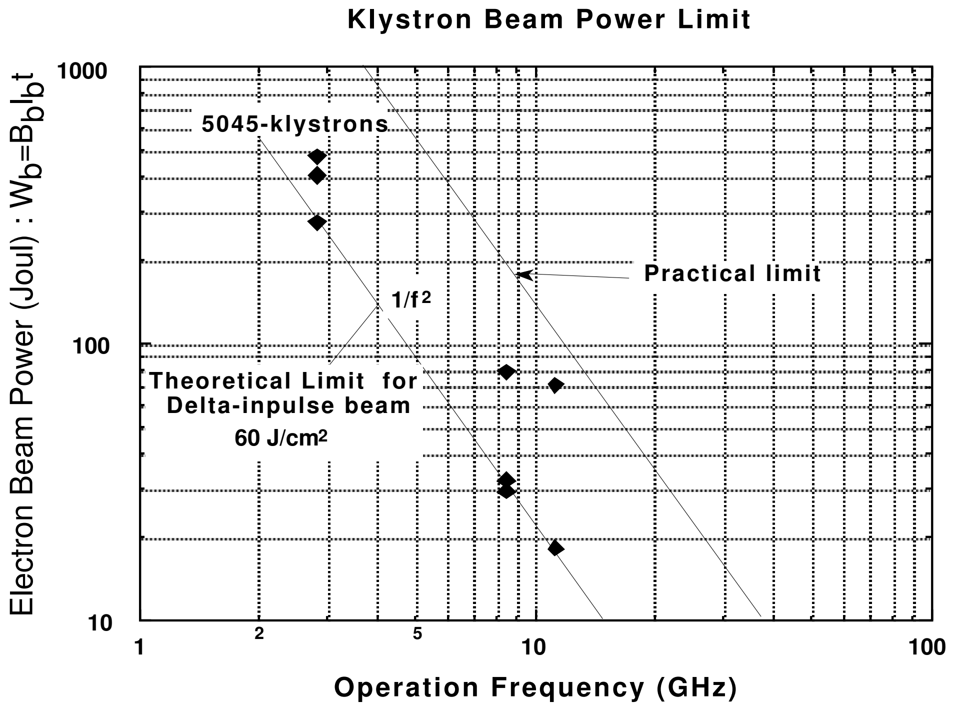

Figure 4.52: Beam power limits of existing klystrons compared with theoretical guesses.

at SLAC uses the gun voltage 320 kV. This voltage is by now standard owing to the R&D works including the new tachnology of the cathode material. Thus, the C-band klystron of the current design seems quite feasible.

Output Cavity The output cavity of klystron extracts the RF energy from the high power driving beam by decelerating the beam. A high voltage is excited in the gap to the same order as the gun voltage, or even higher, because the effective deceleration voltage is reduced by the coupling coefficient of $0.6 \sim 0.8$. In the case of the 5045 klystron, the output cavity voltage reaches 440 kV at the beam voltage of 320 kV. In order to keep good beam coupling, the gap size must be kept much smaller than the wavelength. Therefore, if the gun voltage is constant, the maximum field gradient on the output gap is lineally proportional to the operating frequency. In the 5045 tube, the maximum field gradient is 440 kV/cm at 100 MW output (2 μsec pulse), and no break down was observed. In our C-band tube, the maximum field gradient is 590 kV/cm at 45 MW output. This is 30% higher than the maximum field in the 5045 tube at 100 MW full power operation. Therefore, some R&D works must be done on the output cavity structure.

For this purpose, a new type of cavity "Nose-cone removed pill box cavity"[31] has been proposed for the output cavity structure, which does not have the nose-cones at the gap but has a smooth shape just as a simple pill-box cavity. This cavity can considerably reduce the peak field gradient without loosing beam coupling coefficient. The maximum field gradient in a C-band klystron using this cavity, is expected to be 300 kV/cm. This is much lower than that in 5045 klystron, therefore no HV break down is expected.

Output Ceramic Window The output window, generally made of high purity alumina ceramics, has to be transparent to RF power, while working as a good vacuum seal. It is susceptible to a HV breakdown problem because the breakdown occurs more often on dielectric surface than in a metal-to-metal vacuum gap.

Because the physical dimension of the window is proportional to the RF wavelength, the RF power density passing through a unit area of the alumna ceramics scales quadratically to the operating frequency, and to the electric field gradient linearly. The 5045 klystron uses two windows in parallel, and there have been no severe problems up to 100 MW. The accepable power per one window is 25 MW at C-band if it scales as the wavelength squared. Therefore, it has to be examined if the conventional ceramic window can stand 50 MW and 3.6 μsec pulse power at C-band.

Pulse Compressor

As stated before, the required pulse length into the the accelerating structure is 0.6μsec, which is relatively short as compared to that for the S-band linac. To efficiently generate this pulse directly from a klystron amplifier, a new HV modulator having shorter rise and fall times has to be developed.

One solution to remove this difficulty is to use an "RF pulse compressor". A compressor temporarily stores a long RF pulse of low peak power and, at the end of the pulse, emits a high-peak compressed power by reversing the input RF phase. The SLED-I has been invented at SLAC and successfully used for doubling the beam energy in the SLC project. However, the output pulse has no flat top and thererfore is not applicable to the JLC in which 100 bunches spaced by 2.8nsec must be equally accelerated.

For this purpose, we adopt the SLED-II type compressor, which utilizes a delay line cavity chain instead of a single storage cavity. It generates a flat RF pulse whose duration is just equal to the electrical length of the delay line. In our case, two RF delay lines of 0.6μsec delay time are required. If we use a simple wave guide for this purpose, the lines becomes 90m long. In order to reduce the length, we employ a kind of disk-loaded slow-wave structure. The key issue is how to realize a reasonably short delay line with a tolerable power loss on the wall and in the mode conversion. We plan to use a low loss mode $\mathrm{TE_{01n}}$ and employ a slot damping structure to minimize the mode conversion loss.

The designed compressor achieves 4.2 times the input RF peak power with 70% power efficiency. The input RF pulse length is 3.6μsec, which is long enough for a conventional HV pulse generator.

System Power Efficiency

Expected power efficiencies in the C-band RF system are summarized in Table 4.20. We use the conventional HV modulator, which has 80% pulse efficiency for a few μsec output pulse. To improve this efficiency, we need R&D works to reduce the rise and fall times.

The klystron efficiency is supposed to be 45%, equal to the S-band 5045 klystron. The power efficiency is a function of the perveance of drive beam and is lower for higher perveance beam. It is also a function of the operating frequency, decreasing with frequency. But this dependence is weak and its mechanism is not clear. Therefore, some work will be necessary to keep 45% efficiency.

The focusing coil of klystron also consumes a noticeable fraction of AC power. In order to reduce the coil power, we directly wind a small coil on the drift tube to create 2 kG peak field near the output gap. The required average field is 1 kG, which will be generated by a conventional solenoid or permanent magnet. The expected AC power is 3 kW for conventional magnets.

For the waveguide system, we use the standard rectangular waveguide EIA: WR187 (JIS: WRJ-5) of inner cross-section 47.55 $\times$ 22.15 mm. The power loss in this waveguide is approximately 0.03 dB/m at 5712 MHz. Suppose the average waveguide length from the pulse compressor to the accelerating structure to be 10 m, the power loss becomes 0.3 dB (- 7%). If we can make the waveguide system with reflection loss lower than a few percent at waveguide junction or bends, the total waveguide loss becomes 10%.

Including all the factors, the total power efficiency from AC input to the RF injected into the accelerating structure becomes 22%. This efficiency can be improved up to 30% by future R&D works on the HV modulator, the klystron, and the pulse compressor.

Table 4.21: Number of Linac Units and Power Consumption (two beams)

HV pulse modulator	2090	
Klystron	4180	
Pulse compressor	4180	
Accelerating structure	8360	
Total RF power input to structure	64	MW
Total power efficiency	22	%
Total electric power consumption	291	MW

The Number of Units and Total AC Power Consumption

As listed in Table 4.21, the total number of linac units is 2090 for two beams. Each unit contains one HV pulse modulator, two klystrons, and pulse compressors and four accelerating structures. Because of such a huge number of parts, we need extensive R&D works for reducing their construction cost.

The total RF power input to the structure is 64 MW, and the system power efficiency is 22%, thus the total AC power consumption in the main linac system for two beams is 291 MW.

4.6.3 C-Band Accelerating Structure

In order to get high luminosity under the limited electric power, the multi-bunch acceleration in one RF pulse is essential in the linear collider. However, as described in section 4.5, the multi-bunch instability is expected to be a severe problem, which causes emittance growth and eventually leads to a luminosity loss. A cure of this problem is one of the most important task in our R&D works.

The multi-bunch instability is caused by higher order-mode-resonances in accelerating structures. An electron bunch passing through an accelerating structure generates higher order modes which kick the following bunches and deflect their orbits. If we can extract the electromagnetic power of these modes from the accelerating structure and damp them before the next bunch comes, the multi-bunch instabilities will be suppressed.

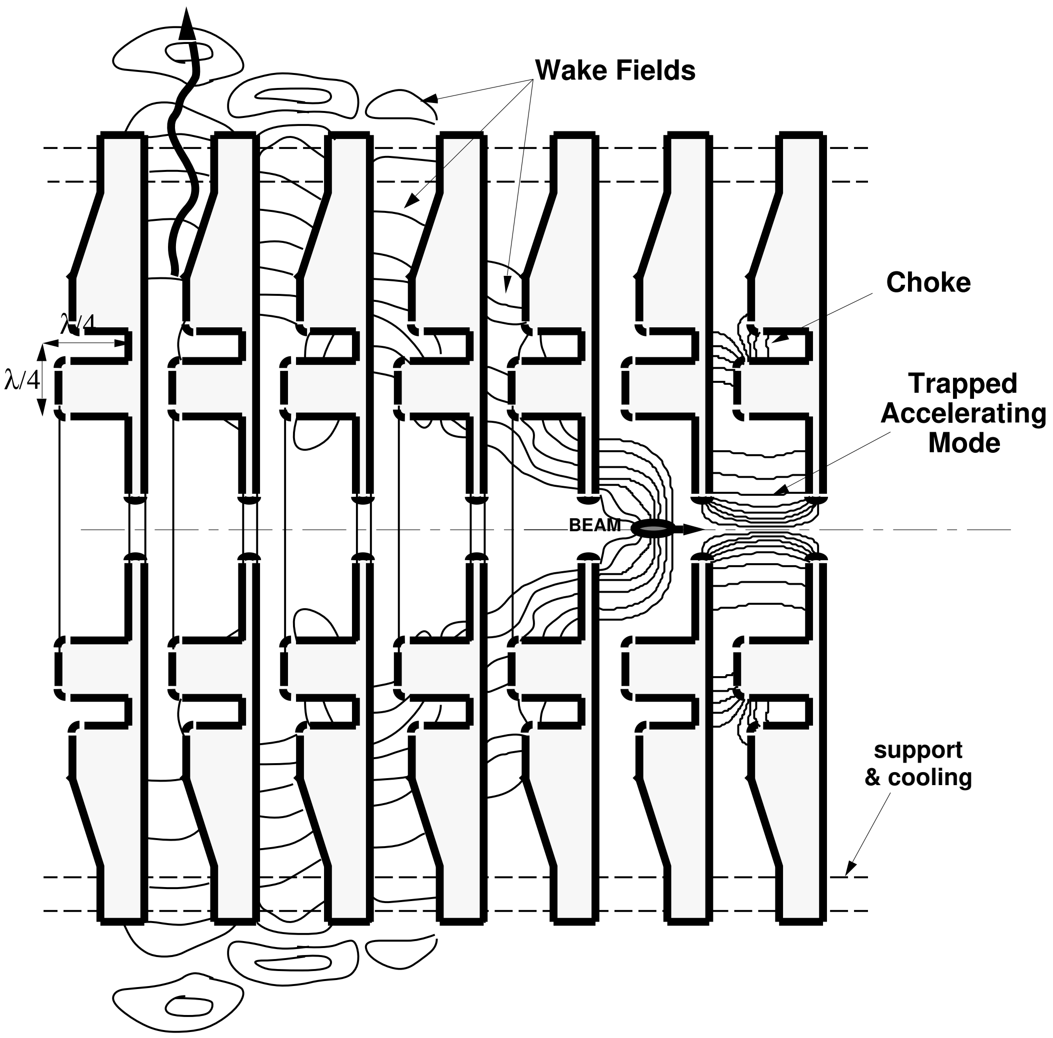

Figure 4.53: Concept of the choke mode cavity with the beam induced field and the accelerating field.

For this purpose, a new type of damped accelerating structure has been proposed[32]. Figure 4.53 illustrates this structure[33]. It consists of a number of disks supported by four rods which are also used as cooling water channels. Because there is no closed metallic boundary around the beam, the wake field immediately propagates outward along the radial line between disks and is eventually absorbed by microwave absorbers mounted on the disks. Therefore, any bunch will not see a wake.

The accelerating mode is trapped inside the structure by means of a choke. The choke length is chosen to be one quarter of the accelerating wavelength to provide an infinitely large impedance, and thus the accelerating RF power is reflected back to the cavity without losing its power by radiation.

A cold model of a single S-band cell has been fabricated and tested[32]. Figure 4.54 shows the measured responce spectrum in comparison with that of a simple pill-box cavity. It can be seen that most of the higher order modes were completely damped. A few modes remain visible, but they are known not to play harmful interaction with the beams. Consequently, this type of cavity will eliminates the multi-bunch problem.

Because this structure has cylindrical symmetry, there is no difficulties in its fabrication. We

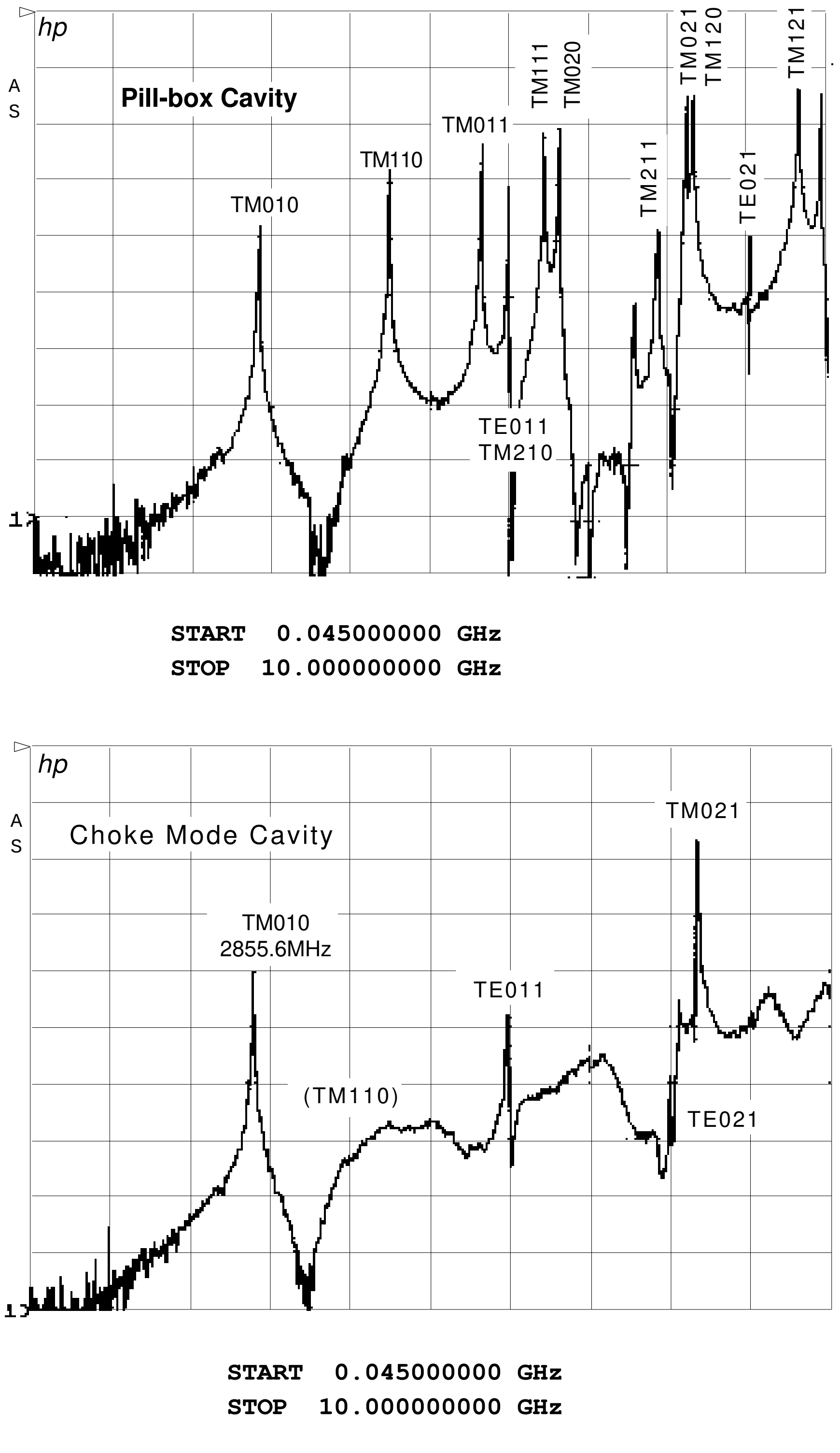

Figure 4.54: Measured responces of the pill-box and the choke mode cavity as a function of the frequency (S-band model).

can fabricate cavity disks from a copper rod or plate on a turning lathe, then stack them together inserting spacers and putting a small SiC disk (microwave absorber) between each pair of the cavity disks, and braise them together. After mounting the power input and output couplers, the accelerating structure unit will be inserted into a vacuum vessel. We will use ~20mmϕ SiC disks as the microwave absorbers, which are expected to be very cheap for mass production. The overall cost will be comparable to that of the conventional disk-loaded structures.

Not everything is perfect, however. A part of the input RF field leaks into the choke, thus increasing the total wall loss and stored energy. As a result, the R/Q and Q values of the accelerating mode decrease by 10% and 15%, respectively as compared to the conventional disk-loaded structures. Therefore, the shunt impedance becomes 25% lower, and we need to input 25% higher RF power to get the same accelerating gradient.

4.7 0.3–0.5 TeV S-band Linac System

4.7.1 S-band Linac

S-band Linac Design

A design study has been carried out for the 300–500 GeV JLC based mostly on conventional S-band RF technologies. In this energy region, especially at 300 GeV, it is expected that the S-band linear collider would be the most realistic machine which can be realized in several years. The S-band JLC consists of the existing components such as the conventional travelling-wave constant-gradient structures of 3.6 m long, 85 MW klystrons and SLED cavities for RF pulse compression. The optimization of the machine parameters is described in Sec. 4.1. The linacs are operated at 50 pps which is synchronized with commercial electricity. The luminosity of 3–4$\times 10^{33}$ is attainable at this repetition rate.

The RF compression system is the key technology to reduce the total number of klystrons and klystron modulators of the main linacs and, therefore, to reduce the total cost. The output pulse from the compression systems like BPC (Binaly Pulse Compression) and SLED-II has a flat top which is desirable in order to equally accelerate many bunches. These systems, however, have relatively long delay lines determined by the sum of the structure filling time and the beam pulse width. Their application to the S-band is unrealistic since the filling time is 500–900 ns and therefore the delay lines would be longer than 150 m.

On the other hand, the conventional SLED cavity used in the SLC, which produces the RF pulse with fast decay, has been thought to be inapplicable to the multi-bunch acceleration. The unequal acceleration due to this decay, however, can be compensated by using cavities driven by slightly different frequencies. It turned out in our study that 70 bunches up to 2.5×10^{10} particles per bunch with the bunch separation of 5.6 ns can be accelerated by this scheme with the resulting bunch-to-bunch energy spread of 0.13–0.14 %.

The unit of the S-band main linac is shown in Fig. 4.55. A klystron feeds the RF power into four 3.6 m long structures via SLED cavity. The peak RF power and the RF pulse width from the klystron are 85 MW and 4.5 μs. At 3 μs after the feed into the SLED cavity, the RF phase is made to reverse. As the results, the RF pulse with 1.5 μs is produced from the SLED cavity. The maximum energy gain produced by the non-square RF pulse is 24.4 MeV/m. However, the net accelerating gain per unit length would be reduced to 20 – 22 MeV/m by heavy beam loading to accelerate intense multi-bunches and by injection timing to obtain the optimum condition of energy compensation.

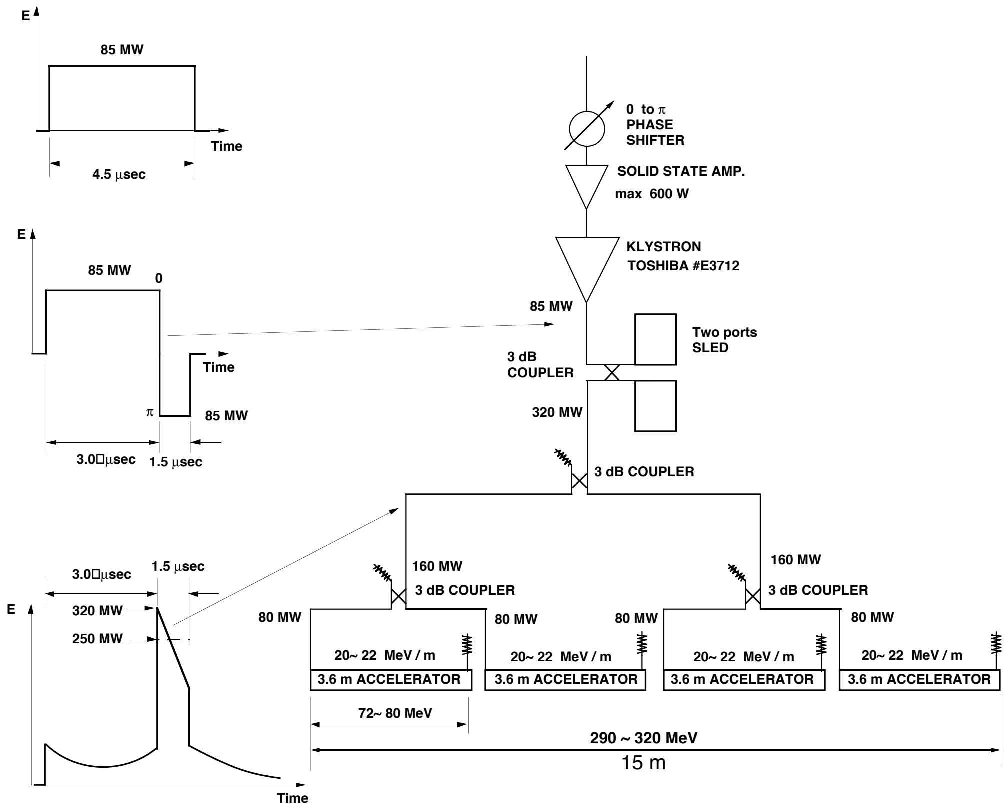

Figure 4.55: Unit of S-band main linac.

Machine Parameters and Parameter Comparison

The linac unit of SLC consists of four 3 m-long accelerating structures and is 12.5 m in length. The DESY 500 GeV linear collider is composed of 2451 units, each of which is about 12.5 m long and consists of two 6 m-long structures and a 130 MW klystron to attain 500 GeV in center-of-mass.

As shown in Fig. 4.55, the S-band JLC is composed of the existing accelerator components, such as 85 MW klystrons, klystron modulators, SLED cavities, and 3.6 m-long accelerating structures which are being tested or fabricated for the ATF (Accelerator Test Facility). The length of the unit is approximately 15 m. The energy gain of the bunches passing through a unit of the linac is approximately 300 MeV with the beam loading. The number of units are 1000 for 300 GeV and 1670 for 500 GeV in center-of-mass energy as shown in Table 4.22. The higher accelerating gradient and the longer unit resulted in a reduction of the total number of linac units, klystrons, and klystron modulators.

Table 4.22: Machine Parameters and Parameter Comparison

C.M.E.	JLC 300 GeV	JLC 400 GeV	JLC 500 GeV	DESY 500 GeV
Total Length of Structures	15 km	20 km	25 km	30 km
Total Length of linear collider	18 km	25 km	30 km	$30+\alpha$ km
Accelerating gradient	22-20 MV/m	22-20 MV/m	22-20 MV/m	17 MeV/m
Total number				
Unit of linac	1000	1350	1670	2451
Klystron and Modulator	1000	1350	1670	2451
Accelerating structure	4000	5400	7680	4902
Structure length	3.6 m	3.6 m	3.6 m	6 m
Peak RF power	85 MW	85 MW	85 MW	130 MW
RF pulse width	4.5 μs	4.5 μs	4.5 μs	2 μs
RF pulse compression	SLED	SLED	SLED	none
Luminosity	3×10^{33}	4×10^{33}	4×10^{33}	2.4×10^{33}
Number of bunch/train	70	70	70	172
Number of particles in a bunch	1.1×10^{10}	1.1×10^{10}	1.1×10^{10}	0.7×10^{10}
Repetition rate (pps)	50	50	50	50
Wall plug power	100 MW	135 MW	167 MW	198 MW
Energy Spread of multi-bunch	0.13 %	0.13 %	0.13 %	0.112 %

Energy Compensation System

The SLED cavity is essential to reducing the total number of klystrons and modulators and, therefore, the cost of the RF system which is the major part of the total cost of the collider. Since the output waveform from a SLED cavity is not a square pulse, an energy compensation system is highly required to accelerate many bunches with a small energy spread less than

1 %. We prepare two different RF turn-on timings into the accelerating structures as shown in Fig. 4.56 and Fig. 4.57. In the first group of linac units, the whole bunches are accelerated by the time the RF front reaches the end cell of the accelerating structure. The last bunch then obtains the highest energy gain. With increasing bunch intensity, the RF turn-on time should be delayed further to compensate the steeper beam-loading slope. In the second group of linac units, the first bunch is accelerated at the time the RF front reaches the end cell. The first bunch obtains highest energy gain than the following bunches. The distribution of linac units in two groups depends on the beam-loading. The ratio of the first and second groups is 1000:103 at 2.50×10^{10} particles per bunch, and 157:100 at 1.0×10^{9} particles per bunch. The energy distribution of the bunches is approximately the cosine curve and the energy spread of the bunches is 2–3 % as shown in Fig. 4.56 and Fig. 4.57. The energy spread can be compressed to 0.13 % by using energy compression units which are driven at 2856 ± 1.27 MHz. The total number of the energy compression units is about 20–30 for 300 GeV in center-of-mass.

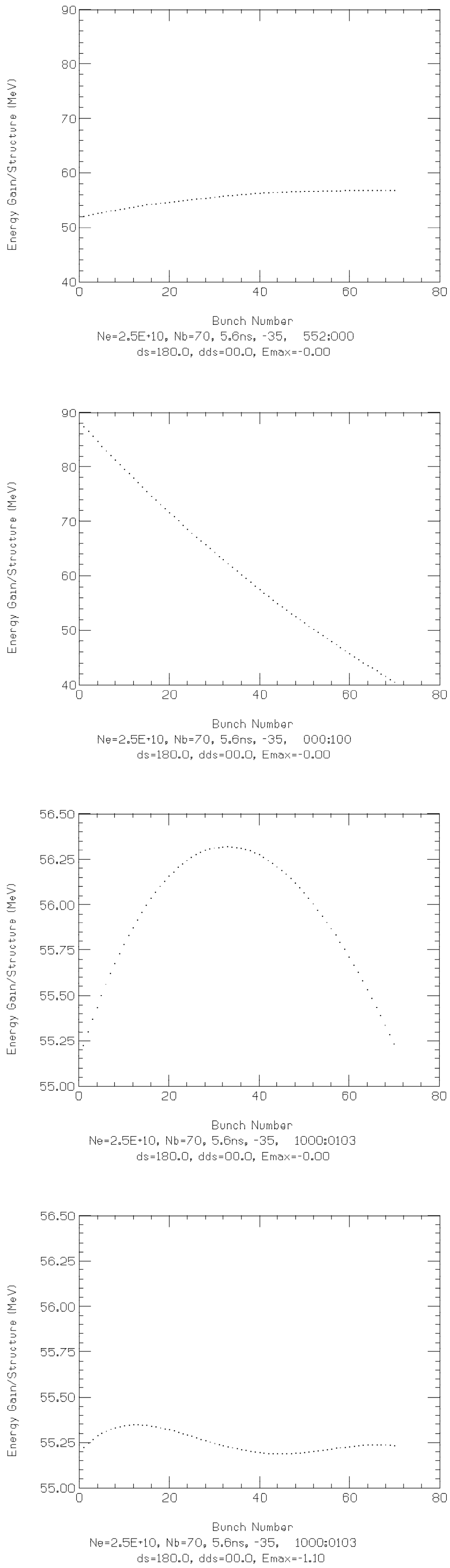

Figure 4.56: Energy spread of multi-bunch. $N_e = 2.5 \times 10^{10}$. Bottom shows the energy distribution after compensation.

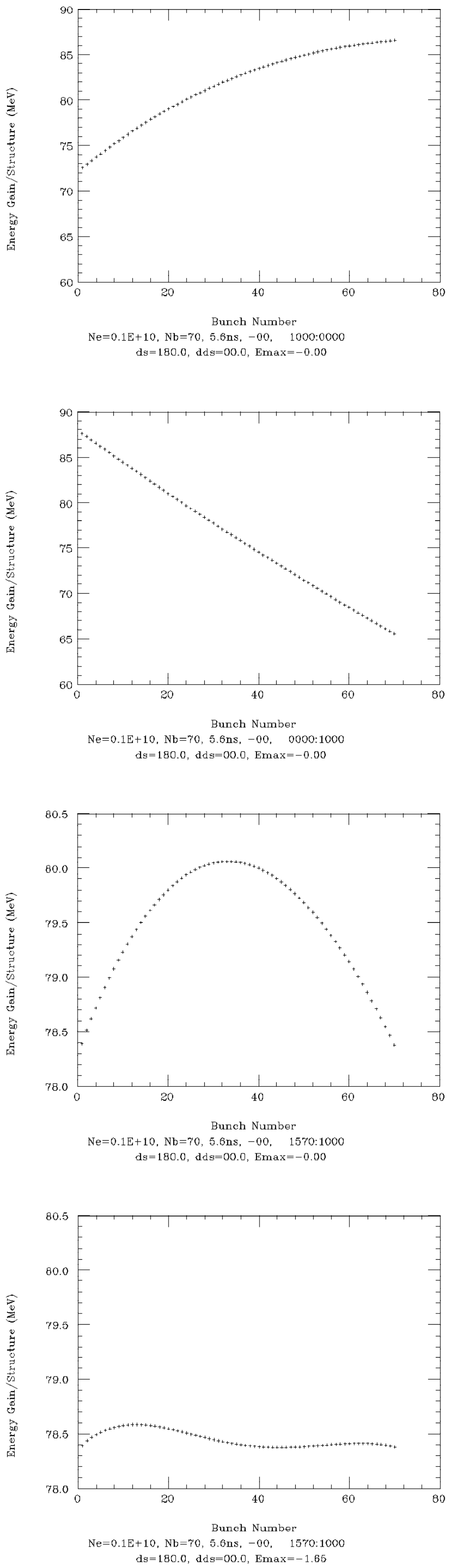

Figure 4.57: Energy spread of multi-bunch. $N_e = 1.0 \times 10^9$. Bottom shows the energy distribution after compensation.

4.7.2 S-band RF System

Outline of RF System

The RF system for the linac unit consists of an 85 MW klystron, a klystron modulator, SLED cavities, and RF waveguides, as shown schematically in Fig. 4.55. The unloaded accelerating gradient is 20 MV/m. The RF power from the klystron is compressed by the SLED system and is divided into four waveguides to feed four 3.6 m-long accelerating structures.

S-band High Power Klystrons

The high power S-band klystrons, Type E3712, have been developed by TOSHIBA Corporation. The tube design has been performed by the computer simulation code FCI. The designed maximum peak power is 100 MW in 1 μs and 80 MW in 4.5 μs pulse duration. The diode voltage is 450 kV at 100 MW and 400 kV at 85 MW peak power. Several klystrons have been used for high gradient experiments in the Nikko experimental hall. These klystrons will be used for the injector to the 1.54 GeV damping ring of the Accelerator Test Facility.

The tube stability is one of the important issues in klystron developments. The measured output power was quite stable at various beam voltages up to 450 kV, various beam focusing currents between 12 A and 20 A, and at various drive power levels.

RF Pulse Compression System (SLED)

SLED cavities established at SLAC are a standard RF compression system at S-band frequencies and are utilized for SLC at SLAC, the LEP injector at CERN, and LAL at ORSAY. The RF energy from the klystron is stored in two TE_{015} high Q cavities and then emitted through the coupling iris into the waveguide to feed the accelerating structure by changing the phase of the RF input pulse from zero to π. The RF pulse of 85 MW of peak power and 4.5 μs in pulse duration builds up the stored RF energy in two high Q (=100,000) cavities, and then the RF power from the klystron triggered at 3.0 μs by a reversal (0 to π) in RF phase. The stored energy inside the cavities is released and combined with the direct RF power from the klystron through a 3–dB directional coupler.

The SLED cavities of SLC have been operated with the input RF power level of 60 MW, pulse duration of 2.7 μs, and repetition rate of 120 pps. At this power level, heavy X-ray is observed from the coupling irises of some cavities due to the RF breakdown occurred occasionally around the irises. In order to reduce the surface field around the coupling iris at 85 MW peak power, a SLED cavity with two sidewall coupling irises has been developed by using the computer simulation cord MAFIA. A simulation showed that the field strength at the irises could be reduced to 34 % by using the two sidewall coupling irises.

Klystron Modulators

The klystrons need a 380 kV pulsed voltage with a 4.5 μs flat top at 85 MW peak power. A line-type modulator has been chosen due to the high efficiency, relatively low cost, and high reliability. A conventional line-type modulator consists of 14 sections of pulse forming network (PFN) and it is resonantly charged and discharged by a single thyratron switch at 50 pps synchronized with the commercial electric line. The regulation of the de-Qing circuit has been chosen to be 5 %. The specifications of the modulators are listed in Table 4.23. Approximately 5 % positive mismatch is used at full voltage for proper operation of the thyratron and the load impedance is about 5 % higher than the output impedance of the modulator. The charging efficiency of the PFN has been estimated to be 95 %.

Table 4.23: Specification of the modulator

Klystron Modulator	
Peak power output	198 MW
Average power output	70 kW
Transformer ratio	1:16
Output pulse voltage	24.8 kV
Load impedance	3.1 Ω
PFN impedance	2.95 Ω
Thyratron anode voltage	51.3 kV
Thyratron current	7984 A
Pulse flat top	4.5 μs
Rise time	0.8 μs
Pulse height deviation from flatness	1.0 % (p–p)
Pulse amplitude drift in short term	$\ll$ 0.5 %
Pulse amplitude drift in long term	$\ll$ 1.0 %
PFN total capacitance	1.19 μF
Repetition rates	50 pps
Efficiency of energy transfer	$\sim$ 85 %
Wall plug power of a modulator	81 MW
Wall plug power of peripheral	
Low level and control	4.5 kW
Klystron focusing coil	8 kW
Klystron heater power	0.5 kW
Klystron driver	1 kW
The others	5 kW
Total wall plug power/RF system	100 kW

4.8 Final Focus System

4.8.1 Overview

The final focus system for the JLC consists of two parts. The first one is a focusing optical system which provides the required nanometer beam spot at the interaction point(IP). The second is a collimator section located between the linac and the focusing optics. We describe the characteristics of the focusing system first in sections 4.8.2 to 4.8.5, then shortly present the collimators in 4.8.6. Figure 4.58 shows the schematic layout of the entire final focus system.

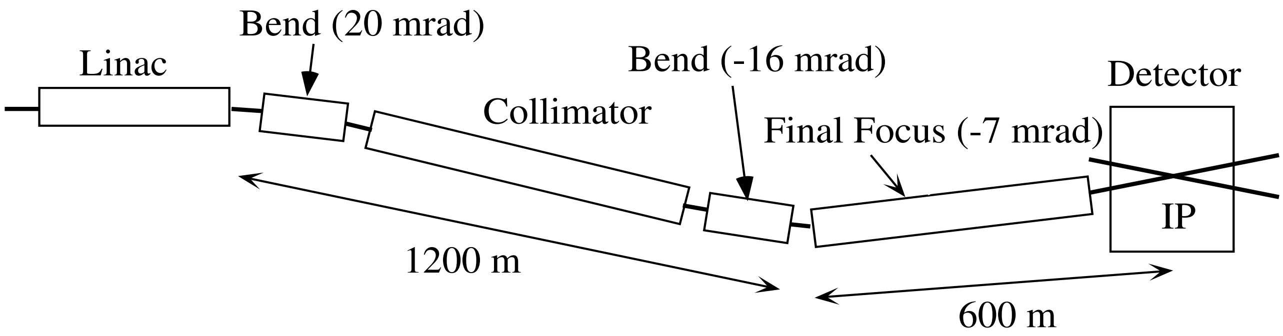

Figure 4.58: A schematic layout of the final focus system.

4.8.2 Design of Optics

The JLC final focus system has the design concept based on the chromaticity-correction scheme with non-interleaved two-family sextupoles[54]. Table 4.24 lists the main parameters of the final focus system for the beam energy 250 GeV. We use the same optical parameters in a lower energy case only with the scaled strengths of magnets. In Table 4.24, the incoming emittances are somewhat larger than those at the damping ring. We design the focusing optics to accept a beam with a certain amount of blow-up and an emittance dilution in the linac. The emittances at IP are larger than the incoming, since they suffer from optical aberrations including the synchrotron radiation in the final focus system. The beta functions at IP are chosen considering the chromaticities and the effects of the synchrotron radiation in the final lenses on the focusing. The focusing components including the final lenses are basically conventional ones, and possible to be built under existing technologies.

Table 4.24: Parameters of the JLC final focus system

Beam energy	E_0	250	GeV
Incoming invariant emittances	$\varepsilon_x/\varepsilon_y$	$3.6 \times 10^{-6}/5.0 \times 10^{-8}$	m
Invariant emittances at IP	$\varepsilon_x/\varepsilon_y$	$3.8 \times 10^{-6}/6.0 \times 10^{-8}$	m
β functions at the IP	β_x^*/β_y^*	10/0.1	mm
Spot sizes at the IP	σ_x^*/σ_y^*	280/3.5	nm
Free area length	ℓ^*	2.5	m
Half aperture of the final quad	a	6.8	mm
Pole-tip field	B_0	1.3	T
Length of the final quad	L_1	2.2	m
Chromaticities of final lenses	ξ_x/ξ_y	3200/43000	
Momentum bandwidth	χ_m	± 0.8	%
Total bend angle	θ	7.1	mrad
Length/beam	L_0	590	m

The optical system is an extension of the FFTB optics[55]. The magnet lattice and the optical functions are shown in Fig. 4.59. We have added several new characteristics on top of the FFTB design. The first one is the long length of the free area for the detector around IP. We set this length ℓ^* to 2.5 m, which is sufficient to place the masks for the background, to

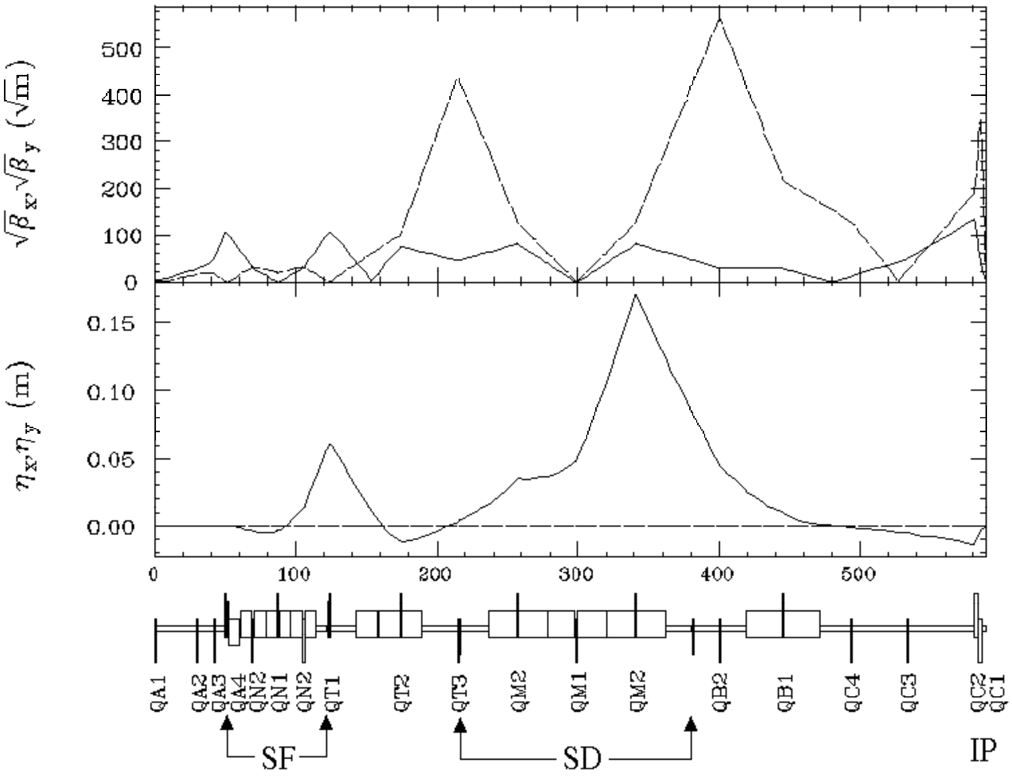

Figure 4.59: Optics of the JLC final focus system.

put BPMs for the beam-beam steering, to make a side-hole at the final quadrupole to let the beam escape after the collision, and to place a super-conducting shield of the quadrupoles for the solenoid field of the detector. Generally a long ℓ^* may increase the chromaticity of the final lenses and decrease the tolerance of the system, but our length 2.5 m is still manageable.

The second new point in the design is the choice of the aperture of the final lenses. In the JLC design these lenses have $30\sigma_x$ and $60\sigma_y$ half apertures. This big ratio to the beam size is necessary to avoid a blow up due to the resistive and geometric impedances of the beam chamber and the pole-tips of the quadrupoles. This big aperture ratio is also required to prevent the synchrotron radiation by large amplitude particles from hitting the pole.

The third change in the design is the unequal horizontal dispersions at the sextupole pair to reduce the chromo-geometric aberrations caused by the breakdown of the sign changer between two sextupoles for off-momentum particles[56]. This odd-dispersion scheme is suitable to extend the momentum bandwidth.

The fourth modification is the number of quadrupoles in the system. We have reduced the total number of quadrupoles in the chromaticity-correction system and in the final transformer. Now the transformer between two sextupoles is not a $-I$ but a π transformer. The beta exchanger between SF and SD families is no longer a simple magni-demagnifier with π phase advances. These changes eliminate unnecessary quadrupoles without any damage on the optical performance. A small number of quadrupoles reduces the tasks for tuning, orbit control, and positioning of the quadrupoles.

4.8.3 Optical Characteristics

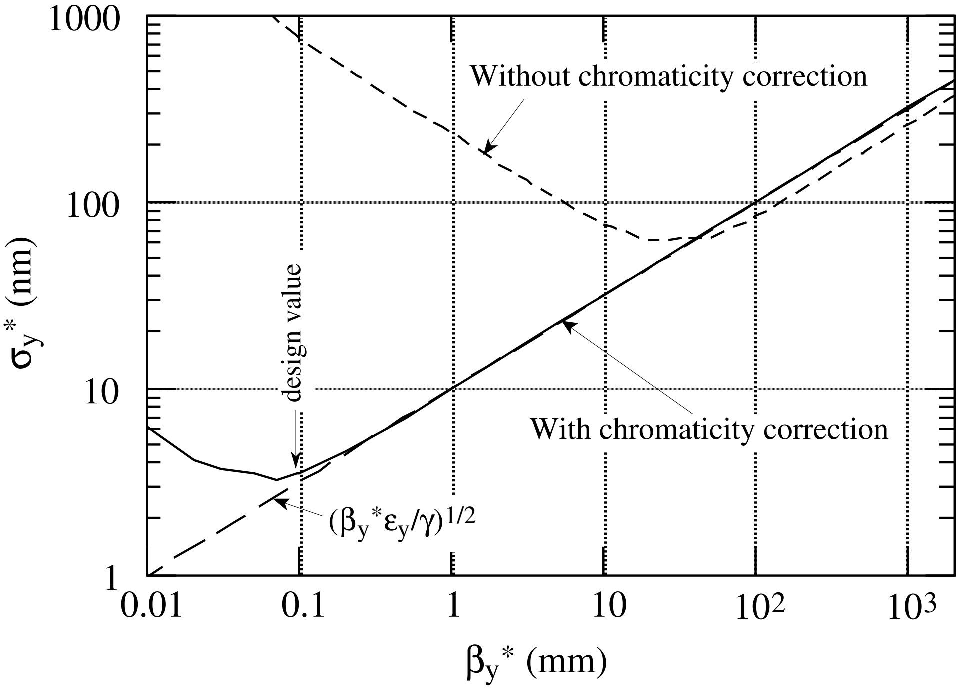

Figure 4.60: The spot size at IP as a function of β_y^*. The chromaticity correction of the JLC final focus system enables focusing down to $\beta_y^* = 0.1$ mm. The improvement of the vertical spot size by the chromaticity correction is 1/160 at the design β_y^*.

In this subsection we present several optical characteristics of the JLC final focus system. First we show the performance of the chromaticity correction in Fig. 4.60.

This figure shows the vertical spot size at IP as a function of β_y^* which we change by the matching at the entrance of the system. While changing β_y^*, the rest of the focusing optics is kept unchanged except the sextupole strengths. The dashed curve represents the spot size when the sextupoles are off. This figure shows that the huge chromaticity of the final doublet blows up the vertical spot 160 times bigger than the design value if we do not have the chromaticity correction. The spot size becomes minimum near the design value of β_y^* as intended by our optimization. For a smaller β_y^*, both chromatic and geometric aberrations increase and prevent further focusing.

The momentum bandwidth of the system is determined by the chromaticity correction and also the optical aberrations, which we will mention later. In this design we set the bandwidth to $\pm 0.8\%$ as required by the global optimization of the JLC parameters. Figure 4.61 shows the spot sizes at IP as functions of the momentum spread of the incoming beam. We have assumed a uniform momentum distribution of the incoming beam.

Figure 4.62 displays the spot sizes at IP as functions of the bending angle. The choice of the bending angle is another important issue on the design stage. In drawing this figure, we re-determined the sextupole strengths every time we change the bending angle. Other optical elements are kept unchanged. If the bending angle is small, the aberrations from sextupoles increase. If the bending angle is large, the effects of the synchrotron radiation in the bending

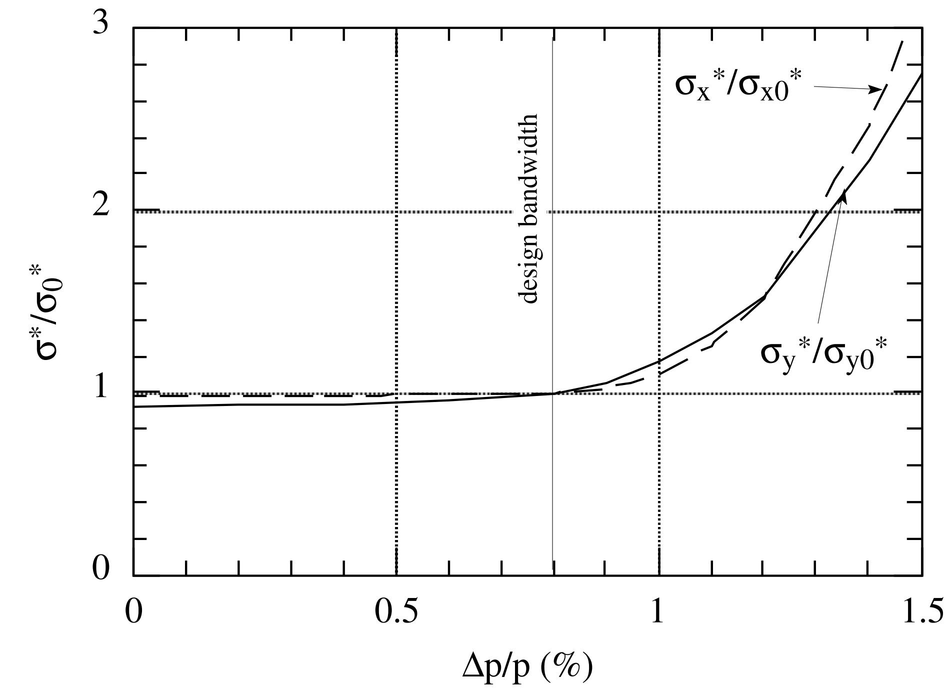

Figure 4.61: The spot sizes at IP as a function of the momentum spread of the incoming beam. The horizontal axis is the half width of the momentum spread with a uniform distribution. The vertical is the ratio of the spot sizes to the design value.

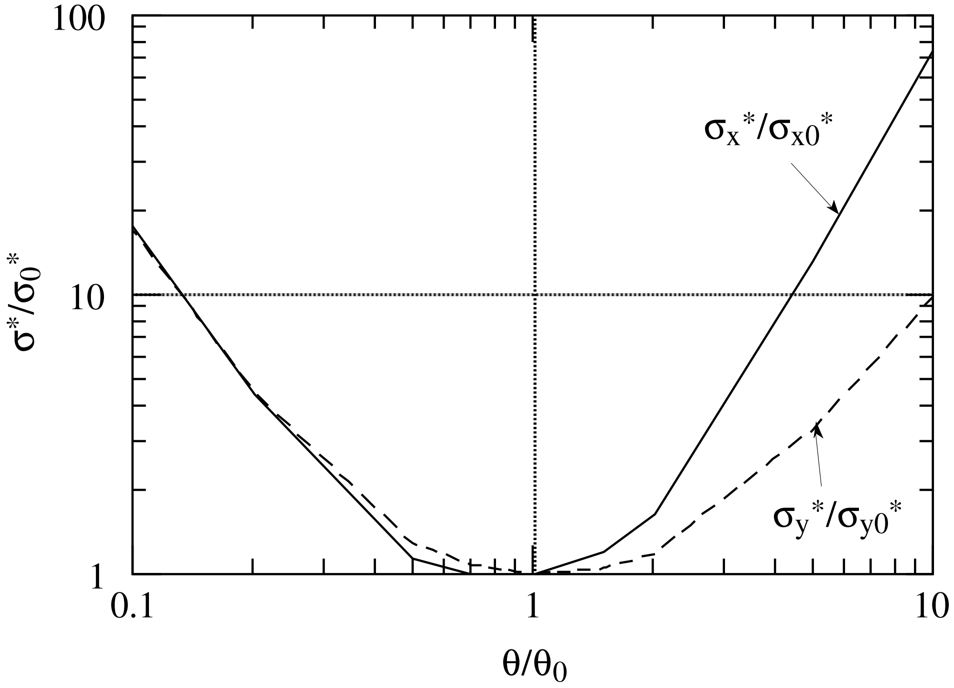

Figure 4.62: The spot sizes at IP as a function of the bending angle. The horizontal axis is the ratio of the bend angle to the design value. The vertical is the ratio of the spot sizes to the design value.

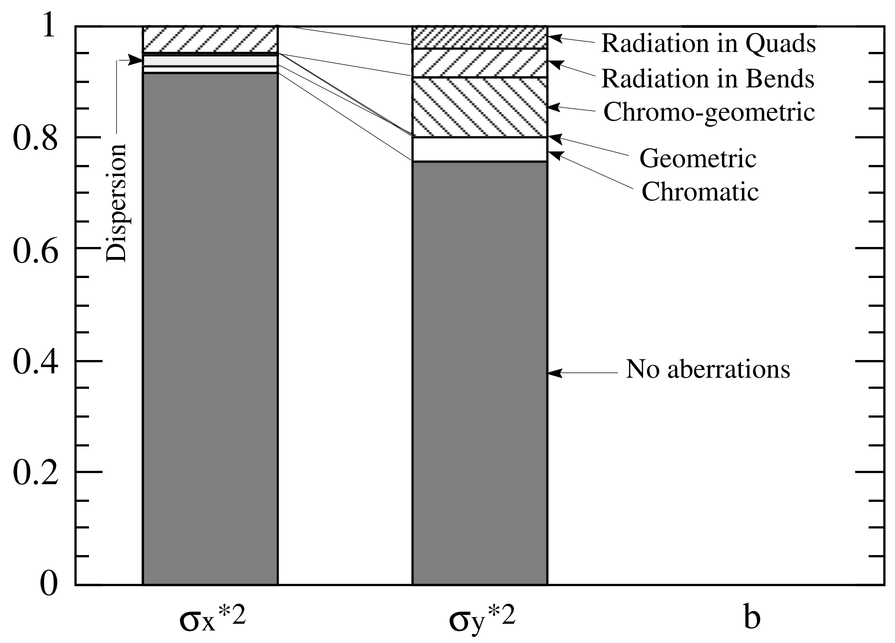

Figure 4.63: The spot sizes at IP have various optical aberrations. Each bar expresses the components of aberrations contained in the design value of the square of the spot size.

magnets blow up the spot sizes. The effect of the radiation is severer in the horizontal in this case. The reason is that the radiation blows up the vertical size through the chromaticity, while producing emittance directly in the horizontal plane. These two effects have different dependences on the bending angle.

Next what we see is the components of the aberrations contained in this design of the optical system, and shown in Fig. 4.63. The part "no aberrations" corresponds to the spot size determined only by the linear optics. Because of the high chromaticity, the vertical spot size has more aberrations compared to the horizontal. One specific aberration in the vertical plane is the chromo-geometric aberration generated by the breakdown of the sign changer of the SD sextupole pairs. The synchrotron radiation in the final doublet also increases the vertical spot. On the other hand, the horizontal higher order dispersion is a special source of the horizontal aberration.

4.8.4 Tolerances

In this subsection we examine four kinds of tolerances for machine errors of quadrupoles and sextupoles. The first one is the steering tolerance shown in Fig. 4.64. The most tight tolerance is for the final quadrupole QC1. If QC1 shifts vertically by 0.2 nm, the spot at IP shifts vertically by $\sigma_y^*/10$, which is about 0.4 nm. The steering error is recovered by the beam-beam steering feedback described in the next section for low frequency vibration. Therefore this tolerance can be understood as that for vibration faster than 10 Hz, which is the limit of the feedback with the beam repetition rate of JLC.

The second tolerance is for the displacement of the magnets to keep the spot sizes unchanged. Figure 4.65 displays the amount for each magnet to increase the spot size by 10 %.

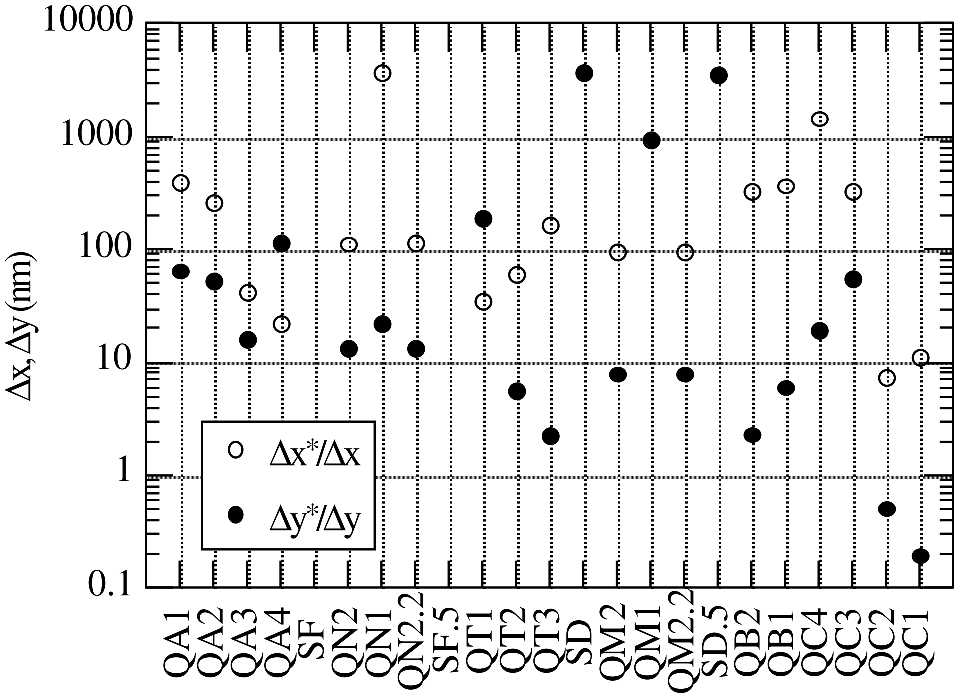

Figure 4.64: The horizontal (blank) and vertical (filled) displacements of the quadrupoles (initial Q) and the sextupoles (initial S) to shift the spot by 1/10 the spot size.

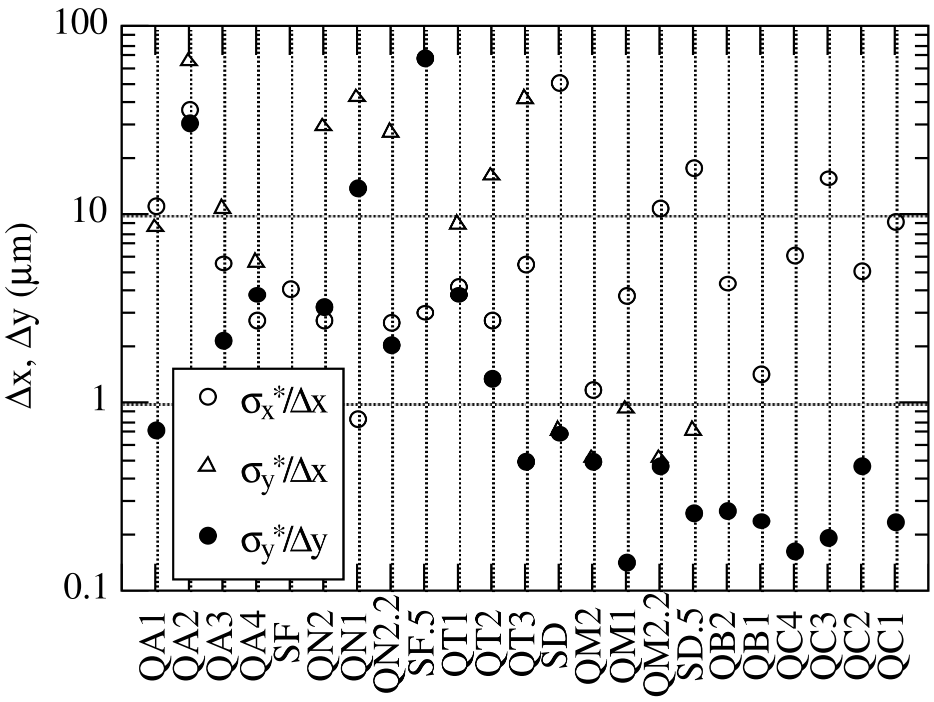

Figure 4.65: The tolerance of the displacements of magnets for the spot sizes at IP. The blank circle is the horizontal displacement which increases the horizontal spot size by 10 %. The triangle is the horizontal displacement to increase the vertical spot by 10 %. The filled circle is the vertical displacement corresponding to 10 % increase of the vertical spot size.

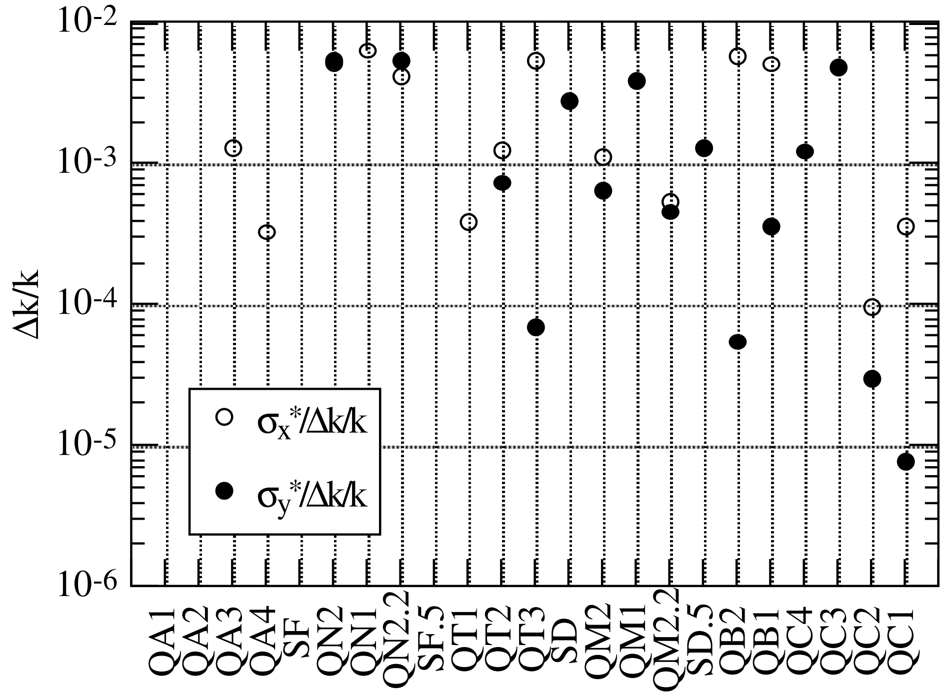

Figure 4.66: The tolerance of the relative strength error of magnets for the spot sizes at IP. The blank and filled correspond to the horizontal and the vertical increases of the spot size by 10 %, respectively.

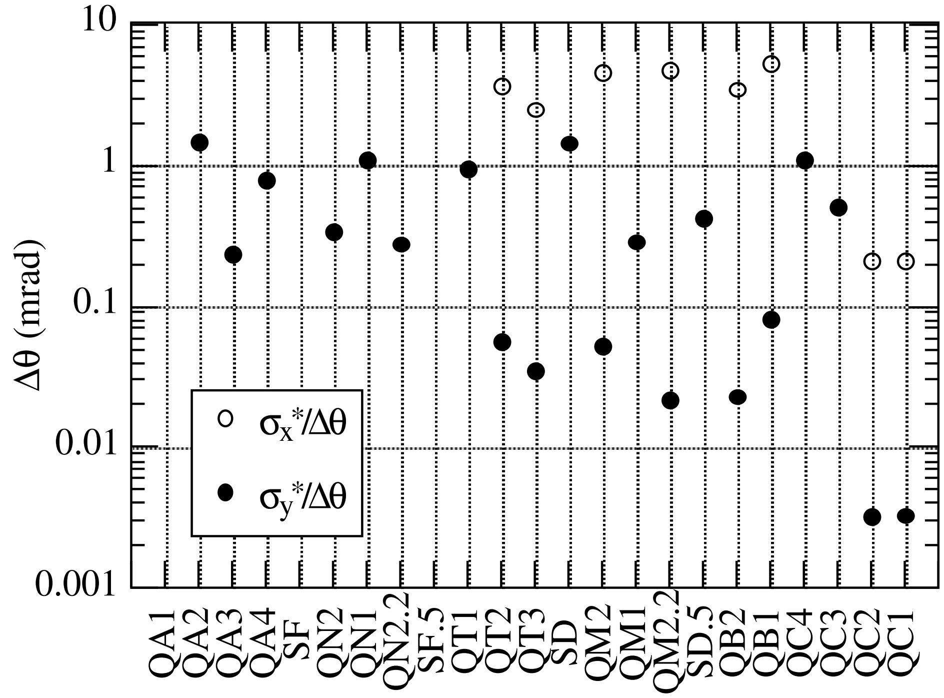

Figure 4.67: The tolerance of the skew rotation error of magnets for the spot sizes at IP. The blank and filled correspond to the horizontal and the vertical increases of the spot size by 10 %, respectively.

This tolerance is tightest in QC4(160 nm) and QM1(140 nm). An orbit feedback using beam position monitors(BPM) at all quadrupoles and sextupoles with an accuracy better than 100 nm maintains the spot as described in the next subsection.

The third kind is the relative strength error shown in Fig. 4.66. Although this tolerance is smallest in QC1, about 1 $\times 10^{-5}$, the stability and the ripple of the power supply at this level are not difficult with the present technologies.

The last tolerance is for the skew rotation angle given in Fig. 4.67.

One may worry that in Fig. 4.65 the vertical tolerance for QC4 is 160 nm which is 1/300 of the vertical beam size at QC4. This does not mean that the beam must always pass this magnet within the accuracy of $\sigma_y/300$. If an orbit error is created at upstream of the entire final focus system, the spot size at IP is much more insensitive to those shown in Fig. 4.65. The reason is that this final focus optics is so designed to make a linear map from the entrance to IP for an incoming particle in a certain range of the transverse amplitudes and the momentum bandwidth. Therefore the tolerance in Fig. 4.65 means the displacement of each magnet relative to all other components of the final focus system. If the entire system moves coherently, the tolerance becomes much looser. Figure 4.68 shows that the tolerance for the launch offset of the incoming beam is nearly 1 σ in both directions. In other words the entire system can shift 1μm in the vertical and 10 μm in the horizontal directions without damaging the spot sizes. The tolerance for the launch angle is similar.

4.8.5 The Nanometer Collision

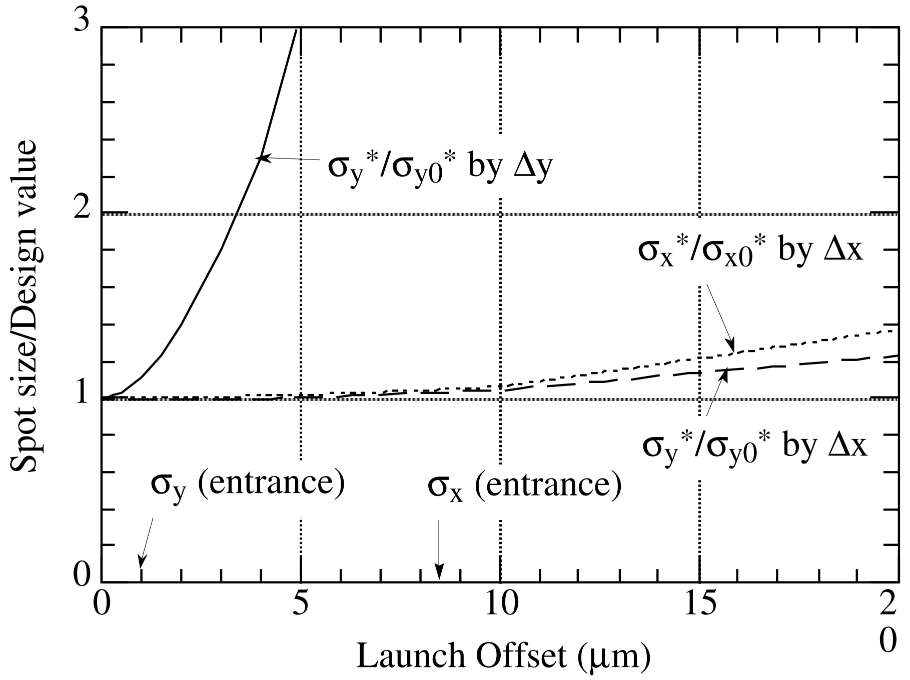

Figure 4.68: The spot sizes at IP normalized by the design values as functions of the launch offset at the entrance of the final focus system.

The key point for a JLC-like future collider is how to maintain the collision of two beams with the nanometer spot size. Basically there are three issues: 1) to keep the head-on collision within an accuracy of a few nanometer, 2) to hold the spot size against possible perturbations, 3) to boot the system into the nanometer regime under various initial machine errors.

A number of studies have been done at SLC to make a stable head-on collision. The basic idea is to sense the deflection of the beams due to the beam-beam kick using beam position monitors (BPMs) located around the IP and to feedback it to the next collision. The beam-beam deflection angle $\Delta y'$ caused by a vertical offset Δy^* at IP is expressed as[57],

$$\Delta y' = \frac{N r_e}{\gamma(\sigma_x^* + \sigma_y^*)} f(D_y) \frac{\Delta y^*}{\sigma_y^*} \ , \tag{4.33}$$

where $f(D_y)$ is a correction by the disruption of the beam with the disruption parameter D_y. This method has been working very well at least for the $1.2\mu\text{m}\times 1.2\mu\text{m}$ SLC spot. In the case of SLC, Eq. 4.33 gives $\Delta y' = 230\ \mu\text{rad} \times (\Delta y^*/\sigma_y^*)$ with $N = 2\times 10^{10}$ and $f(D_y)\sim 1$. In this case the beam is kicked more than 200 μrad, which is easily detected by a standard BPM, when their centers are shifted by $1\sigma_y^*$. One may raise an objection for the applicability of this method to the nanometer case, but in the case of JLC, the sensitivity of the deflection angle to the relative offset at IP is $\Delta y' = 56\ \mu\text{rad} \times (\Delta y^*/\sigma_y^*)$, which is 1/4 of the SLC case ($N = 1\times 10^{10}$, $f(D_y)\sim 0.35$, $D_y = 5$). Therefore it is not much different from the SLC case to detect the offset and to feedback it. The offset of $1\sigma_y^*$ is detectable with a conventional BPM of accuracy 1 μm. In the JLC case one can use all the information from every collision in a pulse to detect the offset. Thus the accuracy can be even better than SLC. The feedback will be active only below 10 Hz because the repetition is 150 Hz. Thus the perturbation beyond 10 Hz cannot be fed back. Recently the vibrations of tunnels and buildings at KEK site have been measured. It is found that the vibration beyond 10 Hz is only a few nanometer even in the daytime. As the reduction of the loss of the luminosity is suppressed by the disruption[57] even if one build JLC-I at KEK, the loss of the luminosity due to the vibrations higher than 10 Hz is only 5 %. One can imagine that it is not difficult to find out a location which is more quiet than the daytime of KEK. Other measurement at UNK also shows that the vibration over 10 Hz is only 0.2 nm[58] The valid range of Eq. 4.33 is $\Delta y^*/\sigma_y^* \lesssim \pm 5$ in the case of $D_y = 5$, but outside that region the beam-beam is still useful to maintain the head-on collision. For instance one can sweep the vertical offset and draw the deflection pattern which tells the location of the center of the collision.

The second issue is to maintain the nanometer spot size. The tightest tolerance for this point is the vibration of the center quadrupole in the vertical chromaticity correction section. If that quadrupole shifts vertically 140 nm relative to the beam, the final vertical spot size increases about 10 %. Therefore we have to keep the vertical beam position at the quadrupole within an order of 10 nm accuracy. Such a high accuracy requires both the accuracy of BPM attached to the quadrupole and the knowledge of the relative offset of the BPM to the center of the quadrupole. Recently T. Shintake and H. Hayano have proposed a design of a BPM whose sensitivity is better than 10 nm. This device will be tested at the FFTB collaboration. If such a high sensitivity BPM becomes available, the determination of the magnetic field center relative to the BPM is possible by a beam-based alignment[59]. When one change the strength of the quadrupole by 0.02 m^{-1}, which causes 10 nm shift of the beam at 50 m downstream the quadrupole if the beam has an offset of 10 nm at the quadrupole. If one use several shots, the required accuracy becomes less. Once the relative location of the magnet center to the BPM is determined, the orbit feedback maintains the final spot size. The tolerances for the other magnets are looser than the quadrupole. An external position sensor and mover system also help the beam-based method.

Orbit feedback system with precise BPMs plays important role in the game to maintain tiny beam size at IP. Increasing the r.m.s. amplitude of the ground vibration, the beam size at IP without orbit correction grows rapidly as shown in Fig 4.69. This beam size blowup is mainly caused by non-vanishing vertical dispersion function at IP, η_y^*. Orbit offsets $\delta y(s')$ at quads and sexts in the final focus system create this dispersion.

$$\begin{aligned}\eta_y^* &= \int^{s^*} ds' \sqrt{\beta^* \beta(s')} \sin(\psi^* - \psi(s')) \\ &\quad [-h_y(s') + k_y(s') \delta y(s')] \,.\end{aligned}$$

When we apply simple orbit correction scheme, in which the strengths of steering correctors are determined so that orbit offsets at quads and sexts vanish, there remains vertical dispersion caused by these steerings. This effect is also seen in Fig. 4.69. This unpleasant effect can be avoided if we apply an additional condition in the determination of strength of steerings[60]. In this scheme, which we call a dispersion-free correction(DFC), the additional condition that the excitation of the steerings does not move the beam position at IP vanishes the dispersion function at IP. In the computer simulation, it is possible to correct this dispersion function completely. Beam sizes after this fictitious correction scheme are also shown in Fig. 4.69. Comparison of these results indicates that our DFC scheme works almost completely for the ground motion less than 3 μm. In this simulation, we have assumed 100 nm BPM accuracy.

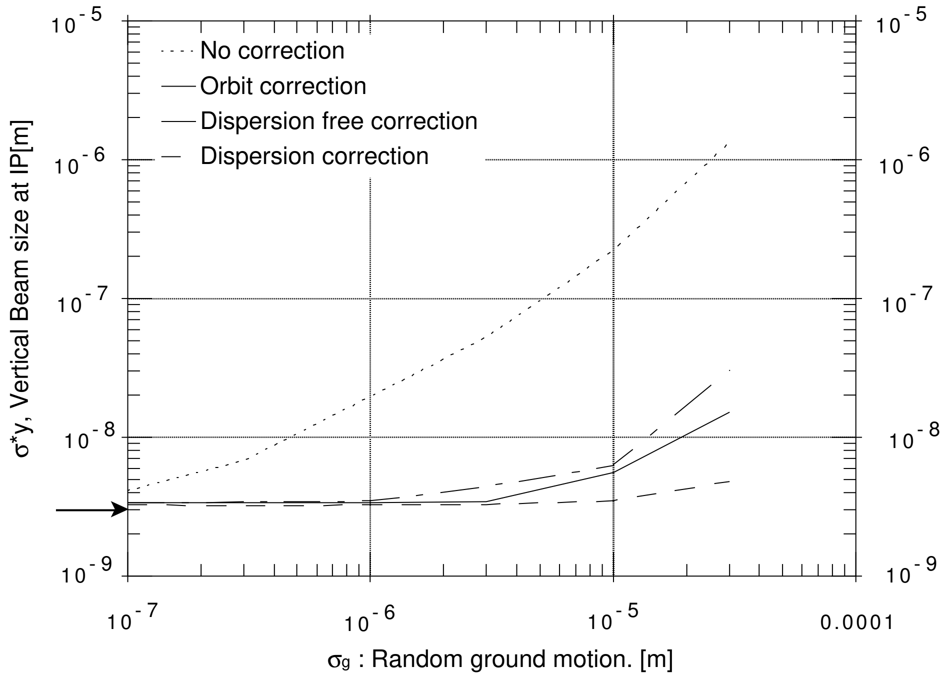

Figure 4.69: The result of computer simulation for the effect of the random ground motion on the beam size at IP. Vertical beam sizes at IP, σ_y*, before and after orbit correction are shown. Arrow on the left vertical axis denotes the design value.

There are, of course, many other sources of perturbation to the spot size. The stability of the power supply is one of them. Some magnets require a relative stability of order of 10^{-6}. A stabilization using an NMR detector is expected to be applied for this purpose.

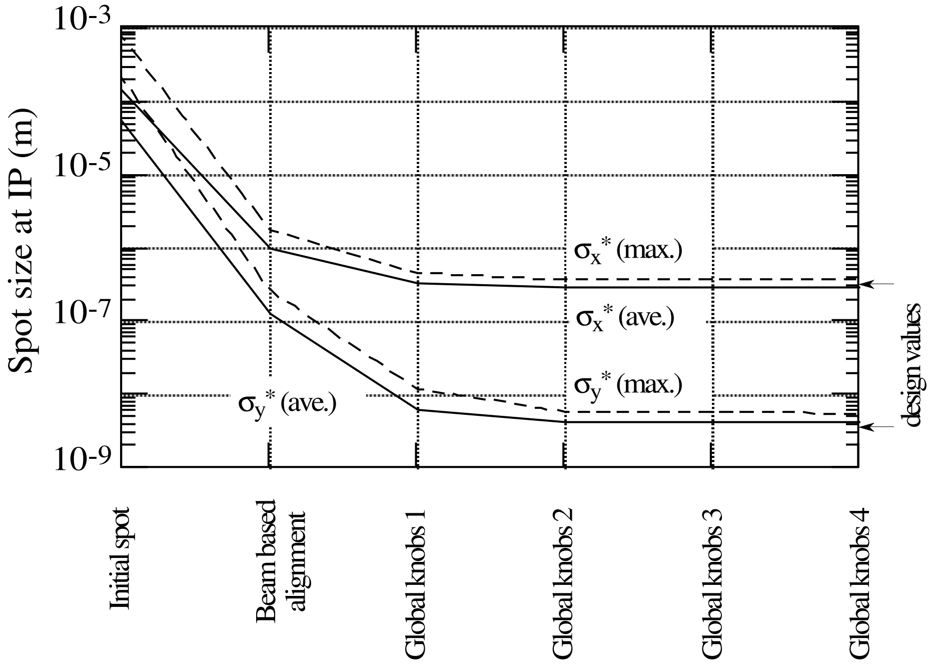

Figure 4.70: Simulation of the tuning of the spot size from initial errors. The beam-based alignment and the global knobs recover the spot sizes. The solid and dashed lines are the average and the maximum of 12 samples, respectively.

The third problem is how to boot the system under several possible initial machine errors. Although there are various ways to do this job as studied at FFTB, we only present here a result with the beam-based alignment method and global knobs. Figure 4.70 shows a result of a simulation. In this simulation we put random Gaussian errors of 100 μm vertical and horizontal displacements, 0.1 % relative strength errors, and 0.1 mrad skew rotation angles to all quadrupoles and sextupoles. The tail of the distribution is cut at 3σ. We did the simulation for 12 different seeds of the random number. At the beginning the spot sizes are bigger than 100μm with these errors. First we applied a beam-based alignment of quadrupoles and sextupoles with BPMs of 2μm accuracy. The beam-based alignment recovers the spot size about 1μm $\times$ 0.1μm. After that we searched the minimum of the spot size by changing several global knobs. The knobs are listed in Table 4.25. We have assumed that the spot size is measurable within 5 % accuracy. After applying the global knobs for 3 cycles, the spot size reaches the design value. The worst vertical spot size among 12 samples is 3.9 nm, while the average is 3.5 nm. This simulation tells that the recovery of the spot size from a conventional level of the initial machine errors is possible if we have a good spot size monitor.

4.8.6 Collimator Section

The JLC final focus system requires a collimation section to cut possible transverse tails of a bunch to protect the detector from the background noise produced by the tail. We expect two major sources of the noise. One is the synchrotron radiation from the tail in the final quadrupoles and the last bend, and another is the shower caused by a particle hitting the pole of the final quadrupole. To avoid both background noises we need a collimator to cut the tail beyond $6\sigma_x$, $35\sigma_y$, and $\Delta p/p < \pm 1.5\%$. The small vertical emittance of JLC makes it

Table 4.25: Global knobs for the tuning of the spot size. H=Horizontal, V=Vertical.

Knobs	Functions to be adjusted at IP
Δx of QB1	H dispersion
Δx of SF1	H focus
Δy, $-\Delta y$, $-0.226\Delta y$ of SF1, SF2, QC4	V dispersion
Δy, $-\Delta y$ of SF1, SF2	V 2nd order dispersion
$\Delta\theta$ of QC1	HV coupling
Δx of SD1, $0.05\Delta x$ of SF1	V focus
Δk of SD1 and SD2	V chromaticity

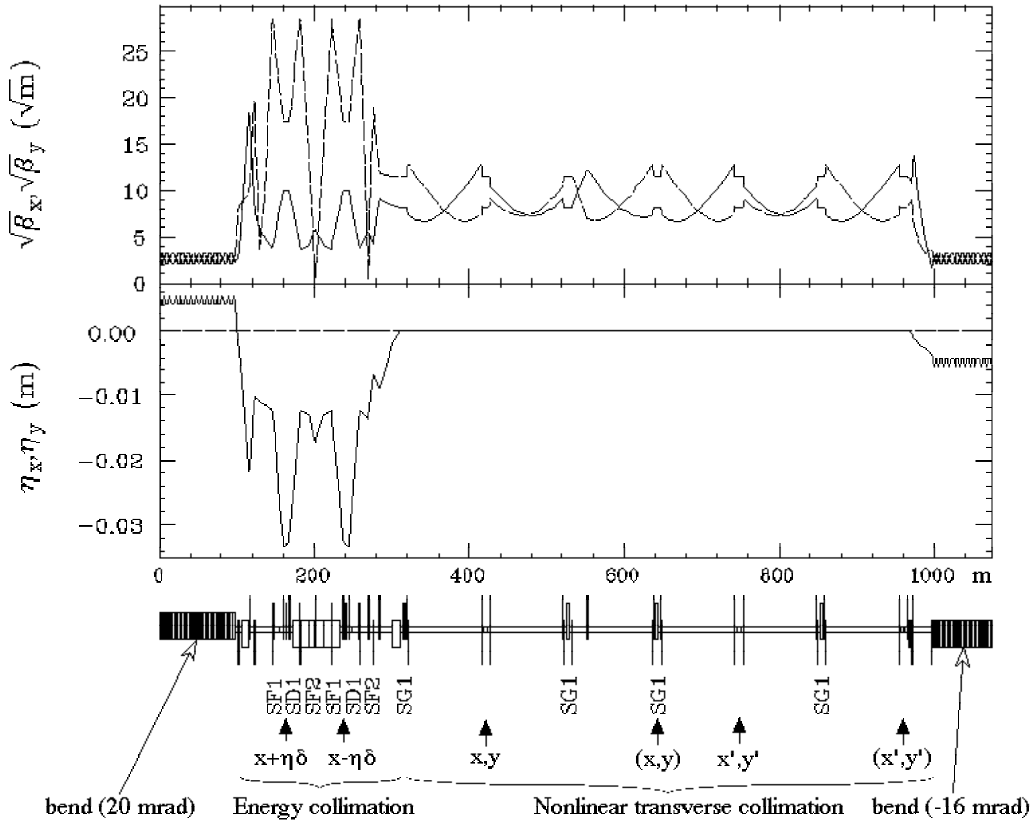

Figure 4.71: Bending and collimation section. The locations of collimators are indicated by filled arrows with their scraping coordinates.

very difficult to place a material very close to the beam because of the resistive and geometric wakefield. Even for a collimator at $35\sigma_y$, we need a special beam optics, so-called a nonlinear collimator[61]. Here we present a design of such a collimator section with parameters listed in Table 4.26. The lattice and the optical functions are shown in Fig. 4.71. This collimation section will be inserted between the linac and the final focus system. This design of the collimation section is also suitable to align two linacs on the same straight line with a finite crossing angle at IP. This design has a capability to install two detectors, because the detector is placed with 15 m horizontal offset to the linacs.

The nonlinear transverse collimation section consists of two identical parts separated by a $\pi/2$ transformer. The first one is the double collimator for (x, y), and the second for (x', y'). Each of them has a sextupole pair connected by a $-I$ transformer. Each sextupole accompanies a collimator at $\pi/2$ downstream. Therefore each part works as a double collimator where the secondary collimator sweeps out the particles reflected by the primary collimator. As shown in Fig. 4.71, the nonlinear collimation section also has several long drift spaces which are suitable to accommodate muon traps.

The horizontal emittance is increased by 3 % due to the synchrotron radiation in the bending magnets. The increase of the vertical emittance due to the sextupoles is negligible.

Table 4.26: Parameters of the JLC collimation section

Bending section 1 & 2		
Bending angle	20 & -16	mrad
Bending radius	4200	m
Tune $\nu_x = \nu_y$	3.5 & 2.75	
Energy collimator		
Acceptance $\Delta p/p$	± 1.5	%
Collimator half aperture	0.5	mm
Beta at col. β_x/β_y	100/300	m
Nonlinear transverse collimator		
Acceptance $x/y = x'/y'$	$\pm 6\sigma_x / \pm 35\sigma_y$	
Collimator half aperture	0.3	mm
Beta at sextupoles β_x/β_y	67/134	m
Sextupole pole tip field	1	T
Sextupole aperture	5	mm
Sextupole length	4	m

4.8.7 Final Focus Quadrupole Magnet

The requirements for final focus quadrupole magnets are very severe: small aperture, very high pole tip field, long pole and small upper limits of higher multipole components, and in addition, a space for exhaust beams are necessary.

The upper limit of relative ratio of sextupole to quadrupole component is $\sim 1 \times 10^{-4}$ at the 10σ radius. Consequently, the machining and assembly tolerance relative to the aperture radius is about $(6 \sim 7) \times 10^{-4}$ which is very difficult to achieve by today's technology. However, the octupole limit is about 1×10^{-3}, which is one order larger than the sextupole limit. Therefore, our strategy is that we take into account only the octupole tolerance at the fabrication stage and cancel out the sextupole component by independently exciting four trim coils.

The structure of the quadrupole magnet is a simple conventional type with four ferromagnetic poles. The design parameters are listed in Table 4.8.7 and the calculated field line is shown in Fig. 4.72.

Table 4.27: The parameters of a conventional type of a final focus quad.

Aperture radius	6.86mm
Pole length	2.4m
Total width	24cm
Pole tip field	1.3T
Current	~6000AT/pole
Total power	39.6kW
Pole and yoke material	FeCo alloy

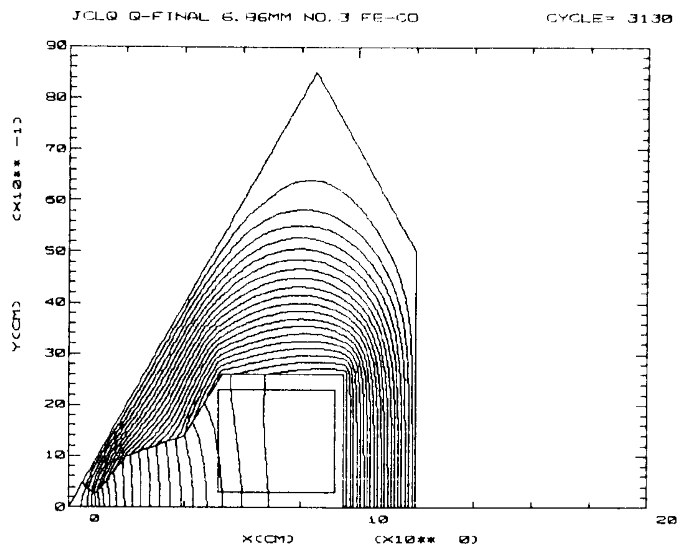

Figure 4.72: Calcurated field line of the octant of the conventional quadrupole magnet.

The calculation shows that the pole tip region is severely saturated so that we need about 1.7 times larger current than the unsaturated case. The current density of the coils is about 14 A/mm^2. In order to limit the temperature rise of coils below 40 degrees, we need cooling water with the pressure drop 8kg/cm^2.

The final focus quad is placed in the field region of the detector solenoid. We have to enclose the quadrupole magnet with a magnetic shield in order to reduce the solenoid field. If we adopt a superconducting quadrupole magnet, the magnetic shield is not needed, which makes the detector structure simple. Since we need a space for the exhaust beam after collision, however, the aperture radius must be large and, therefore, the field on the superconducting coils will be very strong.

A possible design of a superconducting quadrupole magnet is shown in Fig. 4.73 and the parameters are listed in Table 4.8.7. The maximum field on the superconducting wire is about

10.8T, so we have to cool it with superfluid He. In order to get good field quality, four trim coils are also necessary, which are not shown in the figure.

Table 4.28: The parameters of a superconducting final focus quad.

Aperture radius	6.0cm
Coil length	3.5m
Inner radius of coil	8.0cm
Outer radius of cryostat	30cm
Field gradient	117T/m
Current density	$\sim$250A/mm^2
Material of SC wire	NbTi
Coolant	superfluid He ($1.8K$)

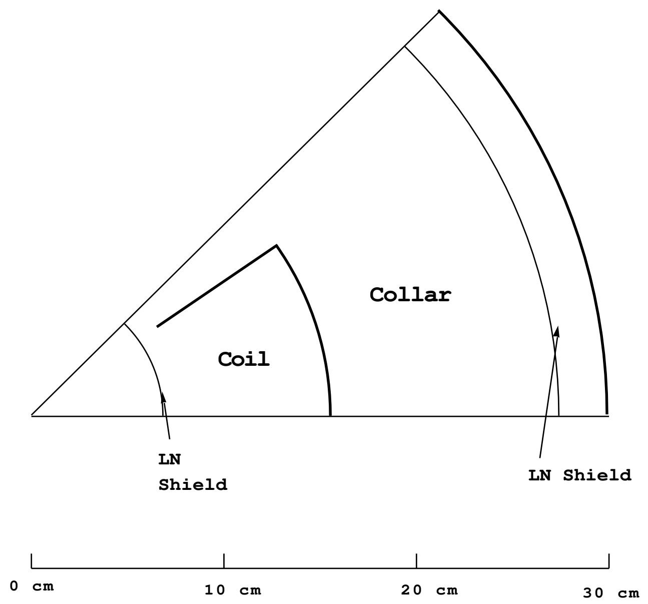

Figure 4.73: The structure of the octant of the superconducting quadrupole magnet.

The requirement for the field stability (current stability) is also severe, about 4×10^{-6} during 4 hours between tunings. As for the current ripple, the upper limit is larger by one order of magnitude, if we use block type magnets. One possible way to make such a stable current power supply is to measure the field of a reference dipole magnet connected in series using NMR and to make a feedback loop. This scheme also works to reduce the current ripple. Thus, the current drift will be reduced to the order of 10^{-6}.